

The relation between HI Gas and Star Formation Properties in Nearby Galaxies

ZHIMIN ZHOU,¹ HONG WU,^{1,2} XU ZHOU,¹ AND JUN MA^{1,2}

¹Key Laboratory of Optical Astronomy, National Astronomical Observatories, Chinese Academy of Sciences, Beijing, 100012, China

²College of Astronomy and Space Sciences, University of Chinese Academy of Sciences, Beijing 100049, China

ABSTRACT

In this paper, we present some correlations of neutral hydrogen (HI) gas and physical properties of galaxies to investigate the role of atomic gas in governing galaxy evolution. We build a HI-detected sample including 70 galaxies that are detected by ALFALFA in a 15 deg² region, and derive their star formation distribution based on the images of H α narrow-band observed here. In general, HI-detected galaxies have low surface density of stellar mass and active star formation. Additionally, most of the galaxies are in good agreement with the star-forming main sequence, consistent with the previous findings. We confirm the dependence of star formation (SF) in galaxies on HI gas at least on global scale, i.e., star formation rate (SFR) generally increases with HI mass, specific star formation rate (SSFR \equiv SFR/M_{*}) increases with HI fraction (f_{HI}) even for a given stellar mass, and HI-based star formation efficiency (SFE) mildly increases with the stellar mass and SFR surface density. Based on the distribution of stellar mass and star formation, we calculate the morphology indices of the sample, and analyze the dependence of f_{HI} and SFE on them. The weak correlations between SFE and morphological indexes imply a weak physical link between HI and star formation in small scale. We find that f_{HI} mildly increases with the asymmetry and decreases with the concentration of galaxies, suggesting that the HI gas supply and its effect are likely correlated with external processes in the extended disks of galaxies.

Keywords: galaxies: evolution — galaxies: star formation — galaxies: ISM

1. INTRODUCTION

The interstellar medium (ISM) is the fuel for the star formation and accretion processes in galaxies, and is fundamental to galaxy formation and evolution. The conversion of gas into stars is the basic process which governs the life of a galaxy. As an important cold ISM component, atomic hydrogen, is widespread in galaxy disks and can be traced by the 21-cm line of neutral hydrogen (HI). HI gas is able to convert to molecular gas H₂ in regions where HI reaches high enough densities and metallicities to become shielded from interstellar ultraviolet (UV) photons (Krumholz 2012). Because molecular gas is directly related to star formation, atomic gas can be regarded as the reservoir of future star formation in a galaxy (Kauffmann 2015). Thus, investigating how and why the atomic gas content of a galaxy varies with

stellar mass and other physical properties can provide initial clues to its growth history.

There have been many works that present the relationships of HI content with galaxy properties, such as stellar mass, color, morphology, star formation, and environment (e.g., Fumagalli & Gavazzi 2008; Cortese et al. 2011; Wang et al. 2011; Hughes et al. 2013). In general, galaxies with more gas are bluer and more actively star forming. Observations have shown the well-known connection between the star formation rate (SFR) and gas content as parameterized by the Kennicutt-Schmidt Law (K-S Law; Kennicutt 1998a; Kennicutt & Evans 2012), indicating that integrated SFR surface density is regulated by the gaseous surface density. Motivated by the K-S star formation law, many investigations have explored the scaling relations of the HI gas fraction with galaxy structure and properties, and calibrated a series of photometric estimators of HI mass fraction with stellar mass, stellar surface mass density, colors, and specific SFR (SSFR \equiv SFR/M_{*}; e.g., Zhang et al. 2009; Catinella et al. 2010; Li et al. 2012). Huang et al. (2012) investigate the global scaling relations and fun-

damental planes linking stars and gas for a sample of HI-bearing galaxies. They found that 96% of their sample belong to the blue cloud, with the average gas fraction $f_{HI} \equiv M_{HI}/M_* \sim 1.5$. Bothwell et al. (2013) found a three-dimensional fundamental relation between stellar mass, gas-phase metallicity, and HI mass, with HI-rich galaxies being more metal poor at a given stellar mass, which is likely more fundamental than the relation between metallicity, SFR and mass.

Blind HI surveys in recent years have produced large, unbiased samples of galaxies selected by HI mass, providing invaluable insights into the research of HI gas in nearby galaxies (see Giovanelli & Haynes 2016, for a review), such as the HI Parkes All-Sky Survey (HIPASS; Barnes et al. 2001; Meyer et al. 2004) and the HI Jodrell All-Sky Survey (HIJASS; Lang et al. 2003). The Arecibo Legacy Fast ALFA (ALFALFA) survey, a wide-field HI survey completed most recently, maps 7000 deg², detects more than 30,000 extragalactic HI sources, and provides the first full census of extragalactic HI line sources over a cosmologically significant volume in the local universe out to $z \sim 0.06$ (Giovanelli et al. 2005; Haynes et al. 2011). Based on ALFALFA catalog, many samples are selected and analyzed in different galaxy regimes. For example, the HighMass sample selected by Huang et al. (2014) includes HI-massive and high-HI-fraction galaxies, the Survey of HI in Extremely Low-mass Dwarfs (SHIELD; Cannon et al. 2011) includes a sample of galaxies with HI masses below $10^7 M_\odot$ outside the Local Group. Besides that, Van Sistine et al. (2016) utilizes a large sample of HI-selected galaxies between 20–100 Mpc from the ALFALFA survey to study star formation in the local universe based on the narrow-band imaging of H α emission line. Gavazzi et al. (2012) completed a similar H α narrow-band imaging survey of an HI line flux-selected sample of Local Supercluster galaxies to probe the role of the environment in shaping the star formation properties of galaxies.

Most of the target selections in previous studies usually focused on certain types of galaxies with specific criteria of physical properties (Wang 2017), and missed a fraction of galaxies which are also detected in HI surveys. Even in the α .40-SDSS-GALEX sample of Huang et al. (2012), there are nearly one-third of galaxies excluded from the parent sample. Therefore, a complete, systematic sample of nearby galaxies is urgently needed to help investigate scaling relations between HI gas and galactic properties, determine the differences in the physical properties of HI-rich and -poor galaxies.

In this paper, we try to present more about the relations between cold gas and star formation in nearby galaxies. We focus on a 15 deg² region of ALFALFA

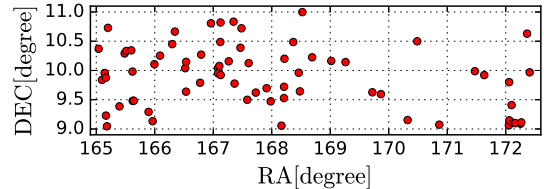


Figure 1. Sky distribution of our sample. The sample includes all of the galaxies detected by ALFALFA survey in the region $11^{\text{h}} \leq \text{R.A.} \leq 11^{\text{h}}30^{\text{m}}$, $9^\circ \leq \text{decl.} \leq 11^\circ$.

survey, select all galaxies detected by ALFALFA in this sky area, take the H α narrow-band imaging to trace their star formation activity, and analyze how the star forming properties correlate with HI gas.

The paper is organized as follows. In Section 2, we introduce in detail the sample selection, the data used in this paper, H α narrow-band imaging, and data reduction. In Section 3 we describe our methodology for measurement the SFR and stellar mass (M_*) of HI sample. Section 4 presents the physical properties of our sample, and analyzes the relations between the HI content, star formation, stellar mass, and galactic morphology. We discuss our findings in Section 5 and summarize the results in Section 6.

In the following, we adopt a standard Λ CDM cosmology with $H_0 = 70 \text{ km s}^{-1} \text{ Mpc}^{-1}$, $\Omega_m = 0.3$, and $\Omega_\Lambda = 0.7$.

2. DATA AND SAMPLE

2.1. Samples and ALFALFA data

The ALFALFA survey presents a database of 21 cm HI line sources over $\sim 7000 \text{ deg}^2$ of the sky at high Galactic latitude, yielding a source density of 5.3 galaxies per deg². This survey covers the recessional velocity range up to 18,000 km s⁻¹ with the resolution of $\sim 5 \text{ km s}^{-1}$, and can detect HI masses as low as $10^6 M_\odot$ and as high as $10^{10.8} M_\odot$ with positional accuracies typically better than 20'' (Haynes et al. 2011). In the ALFALFA catalog, the detections with signal-to-noise ratio S/N > 6.5 are categorized as ‘‘Code 1’’ which are nearly 100% reliable, the sources categorized as ‘‘Code 2’’ have low S/N (< 6.5) but coincide with likely optical counterparts at the same redshift. The HI mass M_{HI} is computed via the formula $M_{\text{HI}} = 2.356 \times 10^5 D_{\text{Mpc}}^2 S_{21}$, where D_{Mpc} is the distance to the galaxy in the unit of Mpc, and S_{21} is the integrated HI line flux density of the source, in Jy km s⁻¹.

Our sample is selected from a $\sim 7.5 \times 2 \text{ deg}^2$ sky region of the ALFALFA survey ($11^{\text{h}} \leq \text{R.A.} \leq 11^{\text{h}}30^{\text{m}}$, $9^\circ \leq \text{decl.} \leq 11^\circ$). It contains all detections with both the code 1 and 2, and adopts the HI measures, distances, and

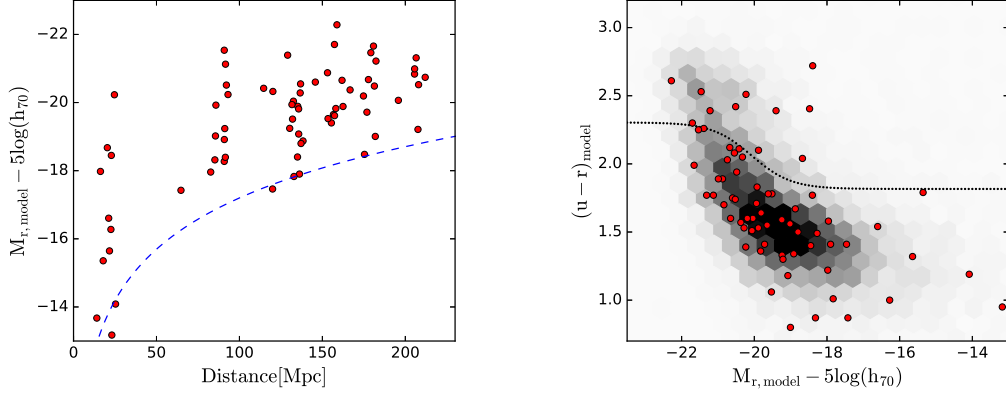


Figure 2. Distribution of our samples in the distance vs. magnitude plane (left panel) and color-magnitude diagram (right panel). The blue curve in the left panel shows the observed flux limits at $m_r=17.77$ magnitude for SDSS legacy galaxy redshift galaxies. In the right panel, the superposed dashed line is the optimum divider separating the red sequence from the blue cloud from Baldry et al. (2004), the gray background depicts the distribution for the ALFALFA-SDSS overlap galaxies shown in Haynes et al. (2011).

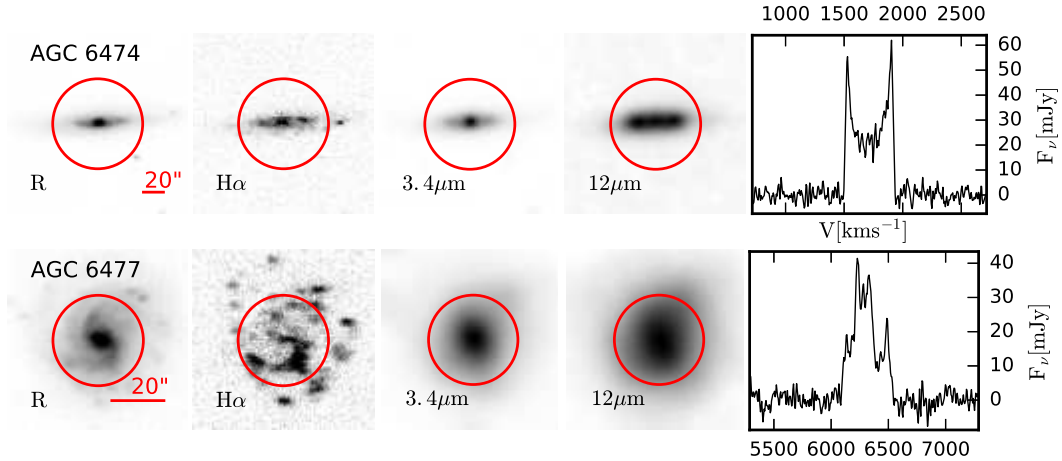


Figure 3. Images and HI spectrum of AGC 6474 (top) and AGC 6477 (bottom). The images of broad-band R , continuum-subtracted narrow-band $H\alpha$, WISE IR 3.4 μ m and 12 μ m, along with the HI Spectrum from ALFALFA are shown from left to right panels, respectively. The galaxy names are specified in the panels. North is up and east is left along with a 20'' scale bar in the first image for each object. Petrosian radii of SDSS r band are overlaid on the images.

HI masses presented in the $\alpha.40$ catalog of Haynes et al. (2011). There are 70 extragalactic HI sources in our sample, 58 with code 1 and 12 with code 2.

Figure 1 presents the distribution of the sample galaxies in the sky region. This region is located in the field near the Virgo cluster, and most of our samples are field galaxies. It should be noted that HI galaxies used in this study are only the objects that can be detected by ALFALFA survey, and the HI-undetected galaxies in the same region may also contain some HI gas, but under the detection limiting of ALFALFA (Haynes et al. 2011). Beside that, based on the results from Gavazzi et al. (2013a), there are no clear difference in the physical

properties for galaxies with projected distance $> 10^\circ$ from M 87. Thus, although our sample is located in the sky region near the Virgo cluster, the effect of coherent structures from Virgo cluster on the property of our galaxies can be negligible.

As shown in Figure 2, most of the galaxies in our sample are located at the distance of 20-230 Mpc with the median distance of ~ 135 Mpc. The right panel of Figure 2 illustrates the distribution of the samples in the color-magnitude diagram with the gray background for all of the ALFALFA-SDSS overlap galaxies shown in Haynes et al. (2011). We also superpose the optimum divider used by Baldry et al. (2004) to separate the red

sequence from the blue cloud. HI-detected galaxies are clearly dominated by blue spiral galaxies.

In Figure A.1, we present the HI profiles of all galaxies, which are derived from ALFALFA. Nearly a half of the sample show the typical two-horned profile of a spiral galaxy, especially for the edge-on galaxies, such as AGC 6474. Besides that, about 10 galaxies have a single peak of the HI profile with velocity width $W50 \leq 50 \text{ km s}^{-1}$, such as AGC 213090 and AGC 6438, which indicates galaxies of sufficiently low mass (Courtois et al. 2009). AGC 6248 is the most anorexic of galaxies in the our sample, its $W50$ is 26 km s^{-1} , and the stellar mass is only $6.3 \times 10^6 M_{\odot}$. There are also some anomalous behaviors in the HI profiles, such as multi-peaks (e.g., AGC 6477, AGC 215241), asymmetric (e.g., AGC 6209, AGC 215236). If true, they are likely derived by the physical process in the galaxy evolution, while some may be due to low signal-to-noise S/N or contamination from near neighbors.

2.2. $H\alpha$ narrow-band observation and data reduction

The $H\alpha$ emission in galaxies can be used as a good star formation tracer (Kennicutt 1998b; Zhu et al. 2008). We performed $H\alpha$ narrow-band observations for the HI-detected galaxies in the spring of 2012. The observations were completed by two instruments on two telescopes, respectively. One is the BAO Faint Object Spectrograph and Camera (BFOSC) mounted on the 2.16m telescope (Fan et al. 2016) at Xinglong Observatory of the National Astronomical Observatories, Chinese Academy of Sciences (NAOC). The other is the Yunnan Faint Object Spectrograph and Camera (YFOSC) mounted on 2.4m telescope (Fan et al. 2015) in the Lijiang observational station of Yunnan observatories, Chinese Academy of Sciences (YNAO). Most objects were observed in photometric conditions: six nights in January and March for BFOSC, and six nights in April for YFOSC.

In the 70 HI-detected galaxies, 43 galaxies were imaged by BFOSC, which has a Lick 1242×1152 CCD detector with the pixel scale of $0''.457 \text{ pixel}^{-1}$ and field of view (FOV) of $9''.46 \times 8''.77$. The others were observed with YFOSC, whose CCD has the FOV of $9''.6 \times 9''.6$ with the pixel scale of $0''.283 \text{ pixel}^{-1}$. The galaxies were imaged with the broad-band R filter and narrow-band filters covering $H\alpha$ emission line (rest-frame wavelength of $\lambda 6563\text{\AA}$). We used the same set of $H\alpha$ filters in BFOSC and YFOSC, which includes 11 narrow-band filters with the central wavelengths between 656.2 and 706.0 nm with an FWHM of 7 nm, corresponding to redshifts of $0 - 22000 \text{ km s}^{-1}$. It should be noted that the $H\alpha$ narrow-band filters also include two $[\text{N II}] \lambda\lambda 6548, 6583$ emission lines, a proper correction for $[\text{N II}]$ emis-

sion is required before the final $H\alpha$ flux is computed. The total exposure times were typically 300 – 600 s for R and 600 – 1800 s for $H\alpha$ based on the observational condition.

We took our data reduction using IRAF¹, and created continuum-subtracted images following the procedure described in Zhou et al. (2015). We summarize this procedure below. First of all, our images were reduced using the standard reduction pipeline, including subtracting overscan and bias, correcting bad pixels and flat fielding, removing cosmic rays, and adding astrometric solutions. Then, flux calibration of broad-band images was made using the field stars cross-matched with SDSS DR10 catalog, whose magnitudes are converted to $UBVRI$ system following on Robert Lupton’s transformation equations on SDSS website². Next, the scaled R -band image as stellar continuum was subtracted from each $H\alpha$ image, and the scale factor for each image was calculated with the flux of a dozen unsaturated field stars near the galaxy. Finally, flux calibration was made for $H\alpha$ images based on the scale factors and effective transmissions of narrow-band and R -band filters.

For the $H\alpha$ images, we then made some corrections before we got the final integrated $H\alpha$ flux. First, a small fraction ($\sim 6\%$) of $H\alpha$ emission is lost in the process of continuum removal (Kennicutt et al. 2008), so we recovered this flux by comparing the scale factors and effective transmissions of narrow-band and R filters. Second, we corrected the Galactic foreground extinction based on the Schlegel et al. (1998) dust maps and the assumption of $R_V = 3.1$ absorbing medium. Then, the deblending from $[\text{N II}]$ was corrected based on the Equation (B1) of Kennicutt et al. (2008). Finally, the uncertainties of our integrated $H\alpha$ fluxes are $\sim 10\%$.

2.3. Ancillary data

To significantly improve the statistics of our samples, a few more data sets are used for analysis or comparison in this paper.

We supplement the photometric data from the *Wide Field Infrared Survey Explorer* (WISE; Wright et al. 2010) to measure SFRs and stellar masses of our HI-detected sample. WISE has mapped the entire sky at 3.4, 4.6, 12, and $22\mu\text{m}$ with an angular resolution of $6''.1, 6''.4, 6''.5, \text{ and } 12''.0$, respectively. We searched the ALLWISE database for detections within $6''$ of the op-

¹ IRAF is the Image Reduction and Analysis Facility written and supported by the IRAF programming group at the National Optical Astronomy Observatories (NOAO) in Tucson, Arizona, which is operated by AURA, Inc. under cooperative agreement with the National Science Foundation

² <http://www.sdss3.org/dr10/algorithms/sdssUBVRITransform.php>

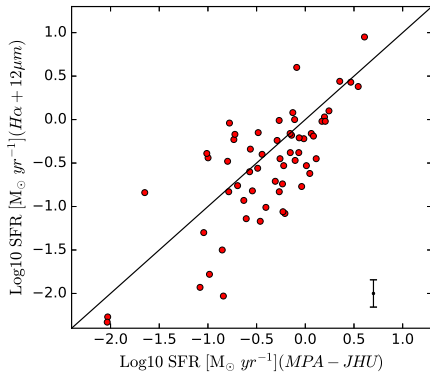


Figure 4. Comparison of $H\alpha + 12\ \mu\text{m}$ based SFR (this work) with MPA-JHU SFRs from SDSS spectroscopic analysis. The solid line marks the one-to-one relation. The error bar indicates the average error of our SFR calculation.

tical coordinates of HI-detected galaxies, and derived their profile-fit photometry magnitudes in these infrared bands.

The Sloan Digital Sky Survey (SDSS; York et al. 2000) provides homogeneous photometric and spectroscopic data of high quality for very large and objectively selected samples of galaxies over one-third of the sky. We derived galaxy properties from the MPA-JHU spectroscopic analysis which presents catalogs of the measurements of absorption line indices and emission line fluxes as well as stellar masses, SFRs, and oxygen abundance for the SDSS-DR7 legacy galaxy redshift sample (Brinchmann et al. 2004; Kauffmann et al. 2003).

Figure 3 shows our images and HI spectrum used for two objects, including continuum-subtracted $H\alpha$, R -broadband, WISE $3.4\ \mu\text{m}$ and $12\ \mu\text{m}$ images. The data for all of the sample can be found in Figure A.1.

3. MEASUREMENTS

We calculate SFRs of the galaxies using the $H\alpha$ emission and WISE $12\ \mu\text{m}$ photometric fluxes with the method of Wen et al. (2014, their Equation 14):

$$\text{SFR}(M_{\odot}\ \text{yr}^{-1}) = 10^{-41.270} \times [L(H\alpha)_{\text{obs}} + 0.038L(12\ \mu\text{m})](\text{erg}\ \text{s}^{-1}). \quad (1)$$

This formula is calibrated with solar abundance and the Salpeter initial mass function (IMF) with a slope of 2.35 for stellar masses in the range $0.1\text{--}100\ M_{\odot}$. Given the uncertainties of our photometric results and SFR calibration we used, the median variation of the SFRs we calculated is ~ 0.033 dex along with most of them ($> 80\%$) less than 0.1 dex.

There are 62 HI-selected galaxies in SDSS MPA-JHU catalog. We compared our result with the global SFRs

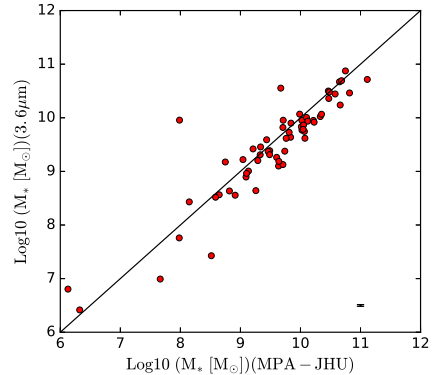


Figure 5. Comparison of WISE $3.4\ \mu\text{m}$ based stellar mass (this work) with MPA-JHU results. The solid line marks the one-to-one relation. The error bar indicates the average error of the calculation.

from the MPA-JHU catalog in Figure 4. The latter is derived based on fiber spectroscopic analysis and aperture correction (Brinchmann et al. 2004). Our SFRs agree well with MPA-JHU SFRs, with no systematic offset and a median difference of 0.03 dex, although noticeable outliers exist. There are some discrepancies between the two SFRs for several galaxies. Large deviations for the outliers are likely due to the differences between the real stellar distribution and models used for aperture correction in Brinchmann et al. (2004).

The stellar mass of our HI-selected galaxies is calculated using WISE $3.4\ \mu\text{m}$ luminosities with the equation in Wen et al. (2013, their Equation 2):

$$\text{Log}_{10}M(M_{\odot}) = -0.04 + 1.12\text{Log}_{10}\nu L_{\nu}[3.4\ \mu\text{m}](L_{\odot}). \quad (2)$$

We compared our results with those derived from SDSS MPA-JHU catalog in Figure 5. MPA-JHU stellar masses are obtained from fits to the photometry with BC03 models (Bruzual & Charlot 2003) spanning a large range in star formation histories (Kauffmann et al. 2003). The stellar masses estimated with the two methods are in excellent agreement for most of the galaxies with a median difference of 0.13 ± 0.28 dex.

Measurements and properties for the 70 galaxies are presented in Table A.1 and A.2. The first table includes the information of the galaxies and the fluxes of HI $H\alpha$ and WISE IR emission. The second one contains the physical properties and morphological parameters for galaxies.

4. ANALYSIS

4.1. Physical properties of HI-detected galaxies

Figure 6 presents the distribution of physical properties of the HI-detected galaxies. The histograms show

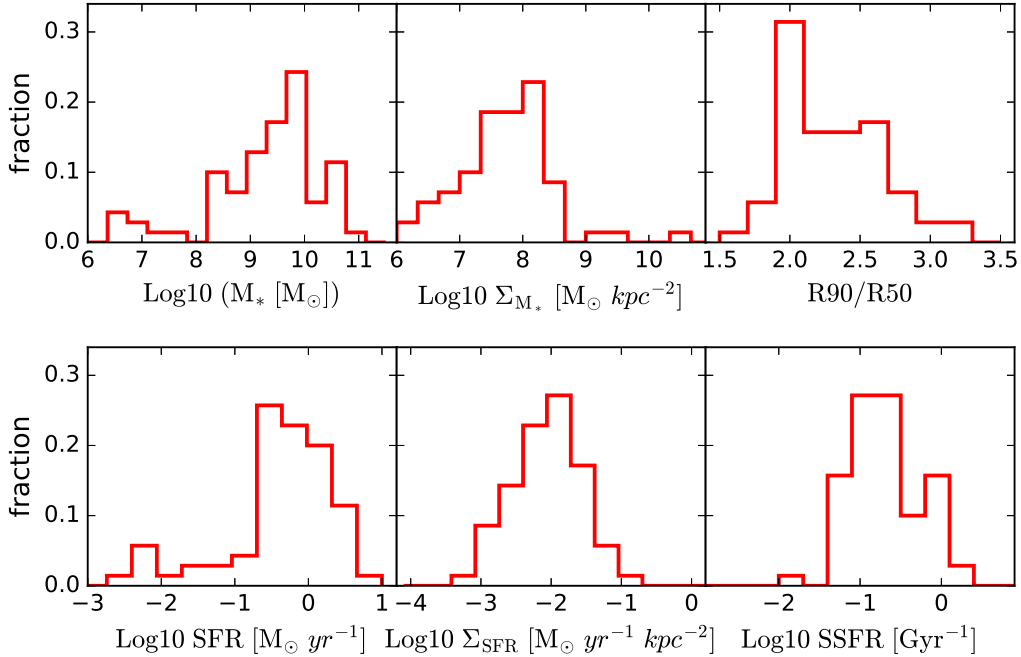


Figure 6. Distribution of the basic properties for the sample. The histograms show the stellar mass M_* , SFR, SSFR, surface densities of stellar mass and SFR, concentration index $R90/R50$ for galaxies in our HI-detected galaxies.

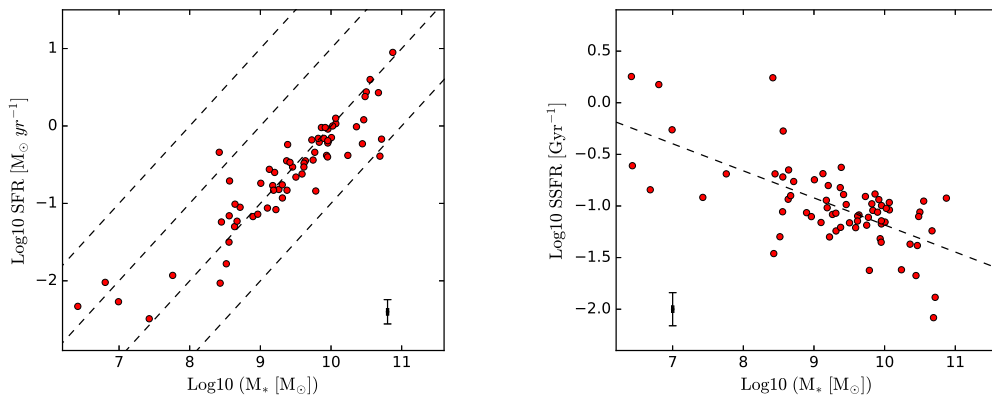


Figure 7. Distributions of our samples in the SFR- M_* (left panel) and SSFR- M_* (right panel) planes. The dashed lines in the left panel mark the positions for SSFR = 10^1 to 10^{-2} Gyr $^{-1}$, top to bottom, with steps of one order of magnitude. In the right panel, the dashed line represents the linear fit for the HI-detected sample.

stellar mass M_* , SFR, SSFR, surface densities of stellar mass and SFR, concentration index. The concentration index is traced by the size ratio, R_{90}/R_{50} , which are the semi-major axes of the ellipses that encompasses 90% and 50% of the SDSS r -band Petrosian flux, respectively. The stellar mass surface density is given by $\Sigma_{M_*} = M_*/(2\pi R_{50}^2)$, and the SFR surface density is given by $\Sigma_{\text{SFR}} = \text{SFR}/(2\pi R_{50}^2)$. The mean stellar mass is $\log_{10}M_* = 9.48$ for the galaxies, and the mean of the stellar mass surface density Σ_{M_*} is $\log_{10}\Sigma_{M_*} = 7.69$. In general, the galaxies in our sample

have active star formation with $\langle \log_{10}\text{SFR} \rangle = -0.28$ and $\langle \log_{10}\text{SSFR} \rangle = 0.71$.

To explore further the dependence of atomic gas on integrated galaxy properties, the distributions of the samples in the SFR- M_* and SSFR- M_* planes are presented in Figure 7. Clearly, the sample of HI-detected galaxies is located following the star-forming main sequence which shows a linear correlation between the logarithm of the SFR and the logarithm of M_* (Brinchmann et al. 2004; Elbaz et al. 2007; Lee et al. 2015). These galaxies

have SSFRs in the range of $0.1 - 1 \text{ Gyr}^{-1}$, consistent with what we found in Figure 6.

For the galaxies in SSFR- M_* plane of Figure 7, we find that SSFRs decrease with increasing stellar mass. We perform robust linear fittings to their relations, and find that the slope is ~ -0.33 for all of the HI-detected sample. The slope is much shallower than that for the relation of non-star-forming galaxies (Bauer et al. 2013).

4.2. Gas scaling relations of the HI-detected galaxies

To demonstrate the role of HI gas in galaxy evolution, we further investigate the correlations between HI and physical properties of galaxies.

4.2.1. The SFR and SSFR in HI-detected Galaxies

Figure 8 shows how SFR and SSFR vary with HI mass (M_{HI}) and HI fraction ($f_{\text{HI}} \equiv M_{\text{HI}}/M_*$) along with the M_* bins. We confirm the previous findings (e.g., Huang et al. 2012) that SFRs generally increase with M_{HI} but decrease with f_{HI} and SSFRs increase with f_{HI} , and these trends still exist in a given M_* bins. The star formation efficiency (SFE $\equiv \text{SFR}/M_{\text{HI}}$) mainly varies in the range of $\log_{10}\text{SFE} = 0.5 - 1.5 \text{ Gyr}^{-1}$. Besides that, we also find the scaling relations of M_{HI} increasing and f_{HI} decreasing with M_* .

However, there are two extreme outliers (IC 676 and IC 698) deviating from the M_{HI} -SFR and f_{HI} -SSFR relations in Figure 8. Both galaxies have much lower f_{HI} or higher SFE than the other counterparts with similar SFR and M_* . IC 676 is a S0 barred galaxy with double star-forming nuclei. It is still unclear if stellar bar or/and galaxy interaction promotes the consumption of HI gas and the formation of the second nucleus. IC 698 is likely a Sa galaxy with obvious irregular spiral structures in the outer disk, and is likely perturbed by galaxy interaction, which may also drive the high SFE of this galaxy.

SFE indicates the efficiency that galaxies convert the Hgas to molecular gas and then stars. Figure 9 presents the variation of HI-based SFE as a function of M_* , SSFR and Σ_{SFR} , respectively. In general, SFE increases slightly with M_* , and galaxies with high HI gas fraction have low SFE, which may indicate a low-efficiency SF law or low-efficient HI-to- H_2 conversion in these galaxies (Huang et al. 2012). There are large scatter in the SSFR-SFE relation, but SFE increases with SSFR at fixed f_{HI} bins. This may be caused by the positive correlation between SFR and SFE. As shown in the right panel of Figure 9, SFE increases with the SFR surface density Σ_{SFR} , suggesting that the efficiency of HI-to- H_2 conversion is high at the region with high Σ_{SFR} .

4.2.2. The relations between HI and galaxy morphology

The morphologies and kinematics of galaxies are able to provide the clues as to the process of gas accretion, and also may determine the gas properties and efficiency of converting HI gas to H_2 and stars (e.g., Blitz & Rosolowsky 2006; Powell et al. 2013). We derive the concentration (C), asymmetry (A) and smoothness (S) indices from our R -band and continuum-subtracted $\text{H}\alpha$ images.

C characterizes the compactness of the light distribution in a galaxy, and is defined to be the ratio of two radii, each of which contains fixed fractions of the total flux in a galaxy (e.g., Kent 1985; Bershady et al. 2000). Here, we use the index C_{42} defined by Kent (1985):

$$C_{42} = 5 \log_{10}(r_{80}/r_{20}), \quad (3)$$

where r_{20} and r_{80} are the radii which contain 20% and 80% of the total luminosity, respectively.

A describes the rotational symmetry of a galaxy system, and is calculated by comparing the galaxy images before and after rotated with the usual rotation angle $\phi = 180 \text{ deg}$ (Abraham et al. 1996; Conselice et al. 2000):

$$A = \frac{\sum |I_{180^\circ} - I_0|}{2 \sum |I_0|}, \quad (4)$$

where I_0 and I_{180° are the intensity distribution in the original image and rotated image with rotation angle of 180° , respectively.

S measures the patchiness of the light distribution in a galaxy, and is defined as the ratio of the amount of light contained in high-frequency structures to its integrated light in the galaxy (Conselice 2003):

$$S = 10 \sum \frac{(I_0 - I_\sigma) - B}{I_0}, \quad (5)$$

where I_0 is the flux distribution of the galaxy, I_σ is also the flux distribution, but smoothed with a filter with σ (here σ is 0.3 times the Petrosian radius of the galaxy), and B is the background value.

The CAS parameters correlate with star formation and major merging activity, and can be used to understand the evolutionary history of a galaxy (Conselice 2003). Here we use the CAS indices from R -band images to characterize the stellar distribution of galaxies, and use the indices from $\text{H}\alpha$ images to characterize the star formation distribution.

Figure 10 presents the correlations of HI fraction f_{HI} and the CAS indices for our HI-detected galaxies. It can be seen that, in general, galaxies with lower concentration or higher asymmetry have higher gas fraction, although the dependence becomes very weak at a given stellar mass. The mild trend of HI fraction with

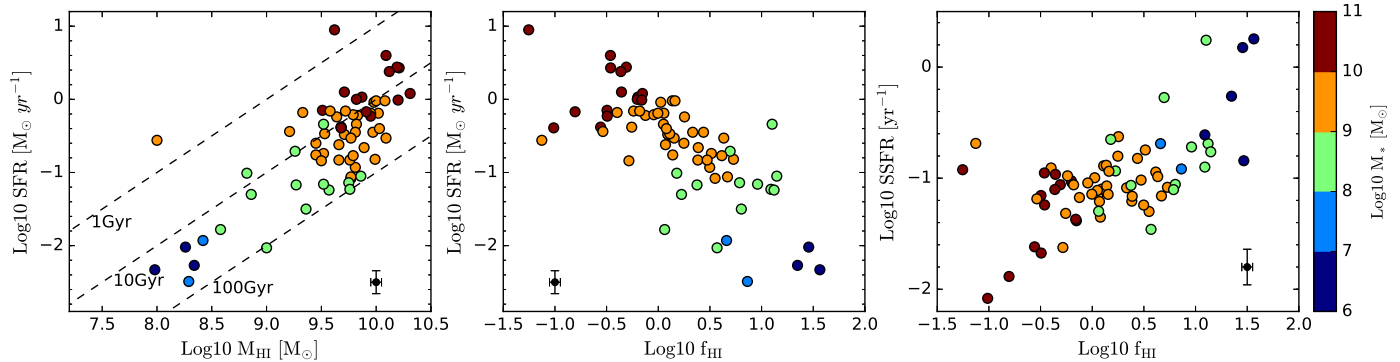


Figure 8. M_{HI} -SFR (left), f_{HI} -SFR (middle), and f_{HI} -SSFR (right) planes for the HI-detected sample. The dashed lines in the left panel are the timescales for depletion of the HI gas reservoir, assuming a constant SFR at the current level, i.e., the reciprocal of the SFE. The galaxies in planes are binned with the stellar mass M_* . The mean errors are marked in each panel.

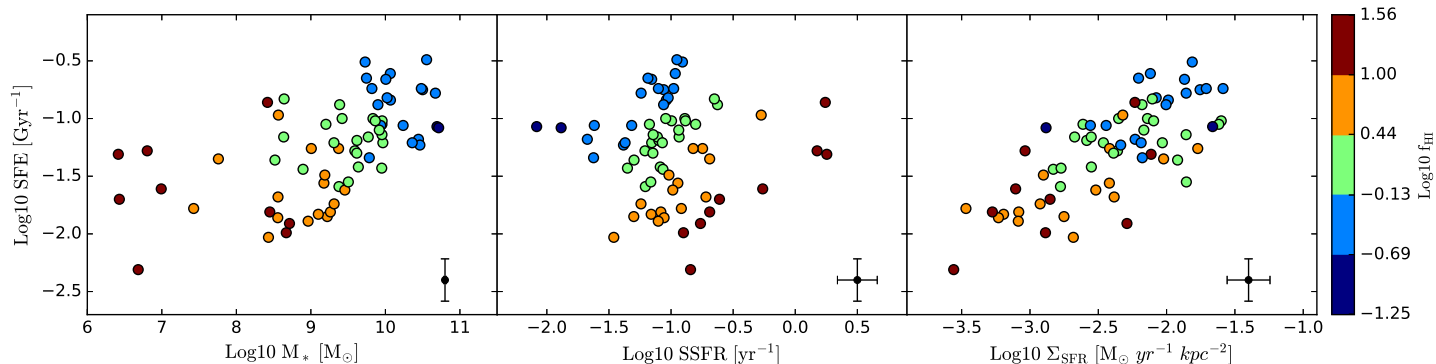


Figure 9. Relation between SFE and galaxy mass M_* (left), SSFR (middle), and SFR (right). Color indicates HI gas fraction f_{HI} .

the *CAS* is likely an indication of external processes or mechanisms that control the gas accretion and supply (Schiminovich et al. 2010). In the bottom three panels of Figure 10, we find little or no obvious trends between f_{HI} and *CAS* indices for star formation distribution in galaxies except f_{HI} vs. $C_{\text{H}\alpha}$, but which is likely driven by the stellar mass. It may suggest that there is little correlation between the spacial distribution of star formation activity and gas fraction due to the smooth process of gas accretion (Wang et al. 2011).

In order to explore the effect of galaxy morphology on SFE, we plot HI-based SFE on a function of *CAS* indices in Figure 11. In each panel, the galaxies are binned with the gas fraction. However, in most of the panels, we find little trends between SFE and the morphology index of stellar mass and star formation. Only weak correlation exists between SFE and concentration C , especially for $C_{\text{H}\alpha}$. For the galaxies with $C < 3.0$, SFE appears to increase with C . While for the objects with $C > 3.0$, the trend is seemingly reversed. The discrepancy between the galaxies with high and low concentration is similar to

the display between HI depletion times and stellar surface density found by Jaskot et al. (2015), and is likely due to the quenching of star formation in more massive galaxies.

5. DISCUSSION

Atomic gas plays an important role in the evolution of galaxies by providing the fuel for star formation activity. The study of HIs essential to gaining a better understanding of the main physical processes in galaxy evolution. In the current work, we have derived the properties of HI-detected galaxies in a ALFALFA sky region, and investigated relations between HI gas content (mass M_{HI} , fraction f_{HI} and SFE) and global galaxy properties such as star formation activity and morphology.

There have been many studies into the question of how the HI properties of galaxies vary with star formation, galaxy structure, and other physical properties (e.g., Roberts & Haynes 1994; Haynes et al. 2011; Toribio et al. 2011a; Huang et al. 2012). As we found

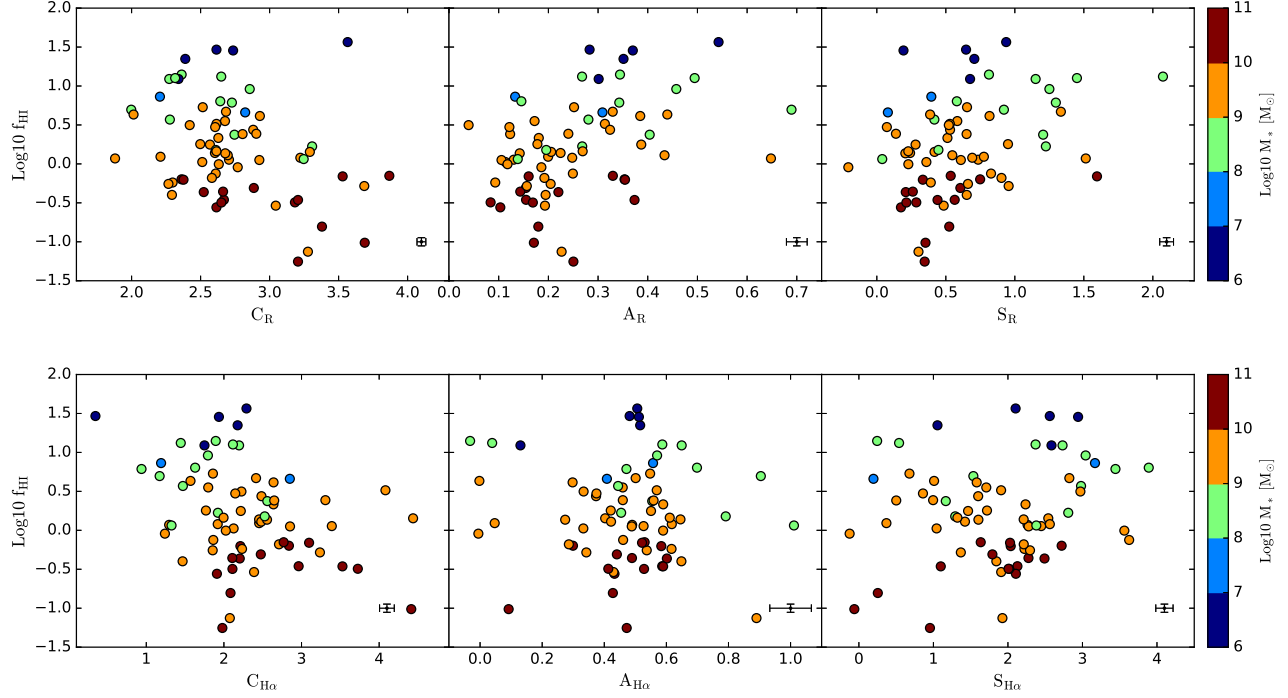


Figure 10. Relationship between HI mass fraction and the morphological parameters for galaxies. The concentration (C), asymmetry (A) and smoothness (S) indices are used and measured from the observed R -band and continuum-subtracted $\text{H}\alpha$ images, and characterize the distributions of stellar continuum (top panels) and star formation (bottom panels). Similar to Figure 8, the galaxies in each plane are binned with the stellar mass M_* .

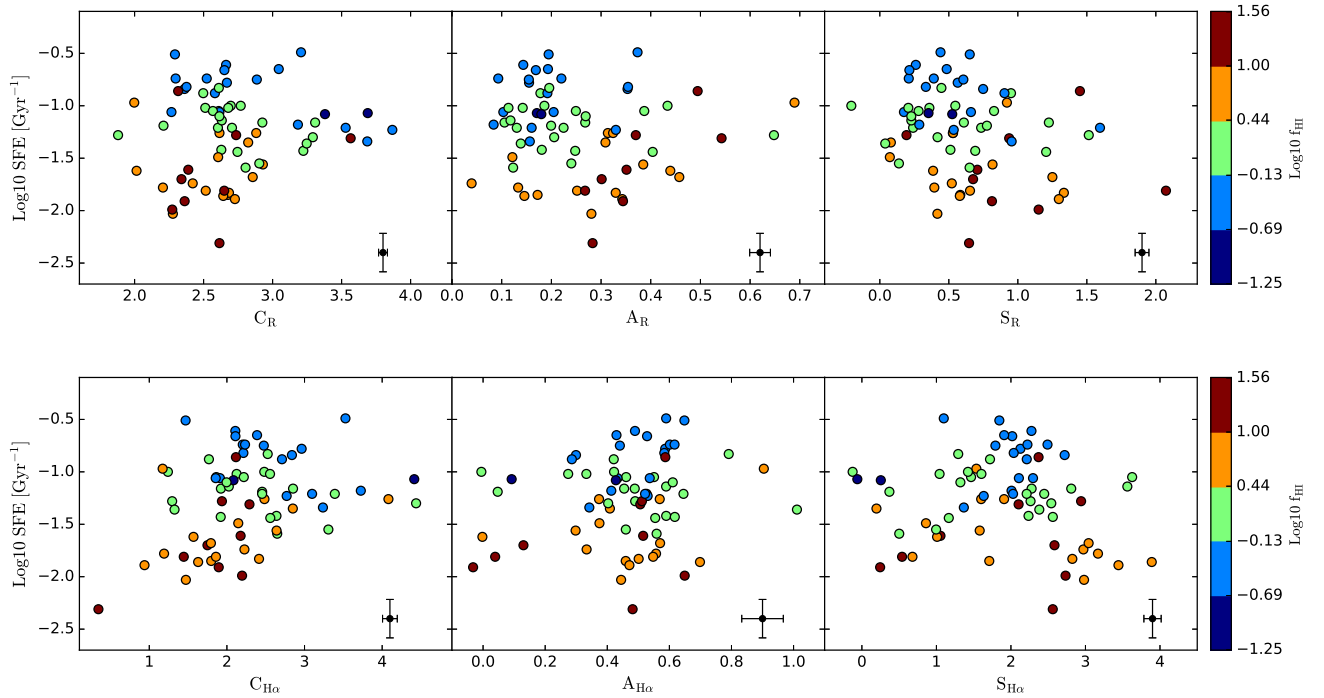


Figure 11. Relationship between HI-based SFE and the morphological parameters for galaxies. The galaxies in each plane are binned with HI mass fraction f_{HI} .

in Figures 2 and 6, HI-detected galaxies are dominated by blue star-forming galaxies, and are strongly biased against the red sequence in the color-magnitude diagram. Many studies have pointed out that there are significant differences between the distributions of physical properties for HI-detected and -undetected galaxies, such as stellar mass surface density, star formation activity, and morphological index (West et al. 2010; Haynes et al. 2011). Similarly, Huang et al. (2012) compared the HI and optically selected samples over the same restricted volume, and found that the HI-selected population is relatively less evolved and has overall higher SFR, higher SSFR, and bluer colors at a given stellar mass, but lower SFE and extinction.

These results are further reinforced by the distributions of our samples in the SFR and SSFR versus stellar mass diagrams. As Figure 7 shows, most of HI-detected galaxies are in good agreement with the star-forming main sequence. In addition, the SSFRs of the our sample show a much shallower decline with increasing stellar mass than the normal non-star-forming galaxies. In agreement with our results, Bauer et al. (2013) found that the dependence of SSFR on stellar mass is steeper for the full sample of galaxies than it is for just the star-forming population. Gavazzi et al. (2013b) found a similar trend in the SSFR-mass diagrams, and identified a four-step sequence of the galaxy quenching process including HI-rich late-type galaxies, HI-poor late-type galaxies, HI-poor galaxies with little star formation, but post-starburst signature, and early-type galaxies.

Recent investigations into the evolutionary properties of galaxies have tried to find possible mechanisms for transforming galaxies from blue actively star-forming systems into red passive systems (e.g., Bothwell et al. 2009; Peng et al. 2015; Davies et al. 2016b). Because HI gas is the initial reservoir where molecular gas and stars are formed subsequently, the star formation in the main Sequence galaxies is supposed to be the produce of relatively stable processes, such as gas inflow and accretion (Davies et al. 2016a), and the low SFRs of the red sequence result from a lack of available gas supply (Bothwell et al. 2009). Saintonge et al. (2016) indicated that if there are no extended HI envelopes or other sources of accretion to replenish the gas reservoirs, galaxies in the main sequence will cease actively forming stars and migrate to the red cloud along with the simultaneous processes in the transformation, such as reduction of the gas fractions, ageing of stellar population and growth of central bulges.

Consistent with these results, Figure 8 shows that SFRs generally increase with HI mass, SSFRs increase with HI fraction even for the galaxies in given stellar

masses, and further confirms the dependence of star formation in galaxies on HI gas. The HI-based SFE also shows an increasing function of stellar mass M_* and Σ_{SFR} (Figure 9). Although Huang et al. (2012) found that SFE remains relatively constant in the high M_* range, we did not find this trend limiting to our sample.

In addition, the f_{HI} and SFE of HI-selected galaxies also show correlations with the distribution of stellar mass and star formation in galaxies. As illustrated in Figures 10 and 11, f_{HI} mildly increases with the asymmetry and decreases with the concentration of galaxies, and SFE mildly increases with the concentration $C_{\text{H}\alpha}$ at the lower end. This may suggest that the HI gas supply and effect are more correlated with external processes or extended disks of galaxies (Wang et al. 2011). Extended galaxies generally have low concentration for the distributions of their stellar mass and star formation, and external processes accrete their ISM to the outer disk which is dominated by HI gas. As a result, the galaxies with lower concentration will have higher gas fraction. Furthermore, SFE decreases with radius across the outer disks of spirals (Bigiel et al. 2010b), thus lower SFE is expected in the galaxies with lower concentration.

While the atomic gas shows a strong correlation with star formation on global scales of galaxies, there seems to be little or no relations between them on smaller scales because star formation is more directly related to molecular gas than atomic gas. As we showed in Figures 10 and 11, f_{HI} and SFE have relatively weak or no connections with the distributions of star formation in galaxies except for the concentration, and the cause might be that the gas richness of galaxies is more closely correlated with the past-averaged star formation in the last Gyr than with the current star formation (Catinella et al. 2010; Kannappan et al. 2013). In addition, more detailed studies on sub-kpc scales show the lack of correlation between surface densities of SFR and HI (e.g., Kennicutt et al. 2007; Bigiel et al. 2008). Wang et al. (2017) indicated that the apparently different behaviors of HI-SFR relations on different scales may be caused by side effects, i.e., HI and SFR both correlate with other physical parameters of galaxies, such as galaxy size and stellar mass, but the physical link between them is intrinsically weak.

Owing to the fact that stars are formed in molecular regions on parsec scales, the above results were somewhat expected. However, HI gas still plays an important role in governing the star formation activity (Fumagalli & Gavazzi 2008; Bigiel et al. 2010b). Besides regulating the formation of giant molecular clouds (Blitz & Rosolowsky 2004), HI is found to correlate with star formation in the outer disks of spirals and in dwarf

galaxies where the ISM is dominated by neutral gas (Bigiel et al. 2010a; Wang et al. 2011). In the investigations of the star formation Schmidt law, Liu et al. (2015) found the total gas density ($H_2 + HI$) shows a steeper function with SFR density than only molecular gas density, especially at the low density regime of molecular gas, indicating that atomic gas may have indirect effect on SF.

While many observational studies have been made, current results for the relation of HI and star formation are still limited by the relatively small number of statistics and lack of deeper data. The star formation tracers used in current works, such as UV, IR, and $H\alpha$ observations, usually have not enough detection limiting, spacial resolution, or sky coverage. Thanks to the recent and upcoming deep surveys, such as the South Galactic Cap u -band Sky Survey (SCUSS; Zhou et al. 2016; Zou et al. 2015), which provide opportunities to measure SFRs of unprecedented large samples with optical u -band data (Zhou et al. 2017). Hence, analyses of larger samples of galaxies based on SCUSS and HI data will be the subject of our future work.

6. SUMMARY

We have investigated the correlations of HI gas and physical properties of galaxies with the aim of exploring the role of HI in governing galaxy evolution. We select all galaxies detected by ALFALFA in a 15 deg^2 sky region as the HI-detected sample, and observe the $H\alpha$ narrow-band imaging to derive their star formation properties. We derive the physical properties of the galaxies and analyze the dependence of star formation and structure on HI gas. Our main results can be summarized as follows:

1. We have obtained M_* , SFR, SSFR, Σ_{SFR} , Σ_{M_*} and concentration index of HI-detected galaxies. In general, our HI-detected galaxies have low Σ_{M_*} and active star formation, consistent with previous findings. Most of the galaxies are in good agreement with the star-forming main sequence in the SFR- M_* plane, and show shallower dependence of SSFR on stellar mass than non-star-forming samples.
2. The dependence of star formation in galaxies on HI gas is confirmed at least on global scale: SFRs generally increase with HI mass but decrease with HI fraction, SSFRs increase with HI fraction even for the galaxies in given stellar mass bins. HI-based SFE is found to increase with the stellar mass and SFR surface density.
3. f_{HI} and SFE of HI-selected galaxies show correlations with the distribution of stellar mass and star formation in galaxies. f_{HI} mildly increases with the asymmetry and decreases with the concentration of galaxies, and SFE mildly increases with the concentration $C_{H\alpha}$ at the lower end, suggesting that the HI gas supply and effect is likely more correlated with external processes or extended disks of galaxies.
4. There are relatively weak or no trends found between f_{HI} , SFE and other morphological indices except the concentration for the distributions of stellar mass and star formation in galaxies, which may be caused by the weak physical link between HI and star formation in small scale and the smooth accretion process of HI gas.

We thank the anonymous referee for numerous valuable suggestions. We gratefully thank Q. Yuan, J. Wang, and C. Lee for useful discussions. This work was supported by the Chinese National Natural Science Foundation grants Nos. 11433005, 11733006, 11673027, 11373035, and 11603034, by National Key R&D Program of China (grant No. 2017YFA0402704) and by the National Basic Research Program of China (973 Program), No. 2014CB845704, 2013CB834902, 2014CB845702, and 2015CB857004.

We acknowledge the support of the kind staff of Lijiang 2.4 m and Xinglong 2.16 m telescopes. Funding for the Lijiang 2.4 m telescope is provided by the Chinese Academy of Sciences and the People's Government of Yunnan Province. The authors would like to acknowledge the work of the entire ALFALFA collaboration team in observing, flagging, and extracting the catalog of galaxies used in this work. Funding for the SDSS and SDSS-II has been provided by the Alfred P. Sloan Foundation, the Participating Institutions, the National Science Foundation, the U.S. Department of Energy, the National Aeronautics and Space Administration, the Japanese Monbukagakusho, the Max Planck Society, and the Higher Education Funding Council for England. The SDSS website is <http://www.sdss.org/>. The SDSS MPA-JHU catalog was produced by a collaboration of researchers (currently or formerly) from the MPA and the JHU. The team is made up of Stephane Charlot, Guinevere Kauffmann and Simon White (MPA), Tim Heckman (JHU), Christy Tremonti (University of Arizona - formerly JHU), and Jarle Brinchmann (Centro de Astrofísica da Universidade do Porto - formerly MPA). This publication also makes use of data products from the *WISE*, which is a joint project of the University of

California, Los Angeles, and the Jet Propulsion Labora-

tory/California Institute of Technology, funded by the National Aeronautics and Space Administration.

REFERENCES

- Abraham, R. G., van den Bergh, S., Glazebrook, K., et al. 1996, *ApJS*, 107, 1
- Baldry, I. K., Glazebrook, K., Brinkmann, J., et al. 2004, *ApJ*, 600, 681
- Barnes, D. G., Staveley-Smith, L., de Blok, W. J. G., et al. 2001, *MNRAS*, 322, 486
- Bauer, A. E., Hopkins, A. M., Gunawardhana, M., et al. 2013, *MNRAS*, 434, 209
- Bershady, M. A., Jangren, J. A., & Conselice, C. J. 2000, *AJ*, 119, 2645
- Bigiel, F., Leroy, A., Seibert, M., et al. 2010, *ApJL*, 720, L31
- Bigiel, F., Leroy, A., Walter, F., et al. 2008, *AJ*, 136, 2846
- Bigiel, F., Leroy, A., Walter, F., et al. 2010, *AJ*, 140, 1194
- Blitz, L., & Rosolowsky, E. 2004, *ApJL*, 612, L29
- Blitz, L., & Rosolowsky, E. 2006, *ApJ*, 650, 933
- Bothwell, M. S., Maiolino, R., Kennicutt, R., et al. 2013, *MNRAS*, 433, 1425
- Bothwell, M. S., Kennicutt, R. C., & Lee, J. C. 2009, *MNRAS*, 400, 154
- Brinchmann, J., Charlot, S., White, S. D. M., et al. 2004, *MNRAS*, 351, 1151
- Bruzual, G., & Charlot, S. 2003, *MNRAS*, 344, 1000
- Cannon, J. M., Giovanelli, R., Haynes, M. P., et al. 2011, *ApJL*, 739, L22
- Catinella, B., Schiminovich, D., Kauffmann, G., et al. 2010, *MNRAS*, 403, 683
- Conselice, C.J. 2003, *ApJS*, 147, 1
- Conselice, C. J., Bershady, M. A., & Jangren, A. 2000, *ApJ*, 529, 886
- Cortese, L., Catinella, B., Boissier, S., Boselli, A., & Heinis, S. 2011, *MNRAS*, 415, 1797
- Courtois, H. M., Tully, R. B., Fisher, J. R., et al. 2009, *AJ*, 138, 1938
- Davies, L. J. M., Driver, S. P., Robotham, A. S. G., et al. 2016, *MNRAS*, 461, 458
- Davies, L. J. M., Robotham, A. S. G., Driver, S. P., et al. 2016, *MNRAS*, 455, 4013
- Elbaz, D., Daddi, E., Le Borgne, D., et al. 2007, *A&A*, 468, 33
- Fan, Y.-F., Bai, J.-M., Zhang, J.-J., et al. 2015, *Research in Astronomy and Astrophysics*, 15, 918
- Fan, Z., Wang, H., Jiang, X., et al. 2016, *PASP*, 128, 115005
- Fumagalli, M., & Gavazzi, G. 2008, *A&A*, 490, 571
- Gavazzi, G., Fumagalli, M., Galardo, V., et al. 2012, *A&A*, 545, A16
- Gavazzi, G., Fumagalli, M., Fossati, M., et al. 2013, *A&A*, 553, A89
- Gavazzi, G., Savorgnan, G., Fossati, M., et al. 2013, *A&A*, 553, A90
- Giovanelli, R., & Haynes, M. P. 2016, *A&A Rv*, 24, 1
- Giovanelli, R., Haynes, M. P., Kent, B. R., et al. 2005, *AJ*, 130, 2598
- Haynes, M. P., Giovanelli, R., Martin, A. M., et al. 2011, *AJ*, 142, 170
- Huang, S., Haynes, M. P., Giovanelli, R., & Brinchmann, J. 2012, *ApJ*, 756, 113
- Huang, S., Haynes, M. P., Giovanelli, R., et al. 2014, *ApJ*, 793, 40
- Hughes, T. M., Cortese, L., Boselli, A., Gavazzi, G., & Davies, J. I. 2013, *A&A*, 550, A115
- Jaskot, A. E., Oey, M. S., Salzer, J. J., et al. 2015, *ApJ*, 808, 66
- Kannappan, S. J., Stark, D. V., Eckert, K. D., et al. 2013, *ApJ*, 777, 42
- Kauffmann, G. 2015, *MNRAS*, 450, 618
- Kauffmann, G., Heckman, T. M., White, S. D. M., et al. 2003, *MNRAS*, 341, 33
- Kennicutt, R. C., Jr. 1998a, *ApJ*, 498, 541
- Kennicutt, R. C., Jr. 1998b, *ARA&A*, 36, 189
- Kennicutt, R. C., & Evans, N. J. 2012, *ARA&A*, 50, 531
- Kennicutt, R. C., Jr., Calzetti, D., Walter, F., et al. 2007, *ApJ*, 671, 333
- Kennicutt, R. C., Jr., Lee, J. C., Funes, S. J., et al. 2008, *ApJS*, 178, 247
- Kent, S. M. 1985, *ApJS*, 59, 115
- Krumholz, M. R. 2012, *ApJ*, 759, 9
- Lang, R. H., Boyce, P. J., Kilborn, V. A., et al. 2003, *MNRAS*, 342, 738
- Lee, N., Sanders, D. B., Casey, C. M., et al. 2015, *ApJ*, 801, 80
- Li, C., Kauffmann, G., Fu, J., et al. 2012, *MNRAS*, 424, 1471
- Liu, L., Gao, Y., & Greve, T. R. 2015, *ApJ*, 805, 31
- Meyer, M. J., Zwaan, M. A., Webster, R. L., et al. 2004, *MNRAS*, 350, 1195
- Peng, Y., Maiolino, R., & Cochrane, R. 2015, *Nature*, 521, 192
- Roberts, M. S., & Haynes, M. P. 1994, *ARA&A*, 32, 115

- Powell, L. C., Bournaud, F., Chapon, D., & Teyssier, R. 2013, *MNRAS*, 434, 1028
- Saintonge, A., Catinella, B., Cortese, L., et al. 2016, *MNRAS*, 462, 1749
- Schiminovich, D., Catinella, B., Kauffmann, G., et al. 2010, *MNRAS*, 408, 919
- Schlegel, D. J., Finkbeiner, D. P., & Davis, M. 1998, *ApJ*, 500, 525
- Toribio, M. C., Solanes, J. M., Giovanelli, R., Haynes, M. P., & Masters, K. L. 2011, *ApJ*, 732, 92
- Van Sistine, A., Salzer, J. J., Sugden, A., et al. 2016, *ApJ*, 824, 25
- Wang, J., Kauffmann, G., Overzier, R., et al. 2011, *MNRAS*, 412, 1081
- Wang, J. 2017, *Scientia Sinica Physica, Mechanica & Astronomica*, 47, 049809
- Wang, J., Koribalski, B. S., Jarrett, T. H., et al. 2017, *MNRAS*, 472, 3029
- Wen, X.-Q., Wu, H., Zhu, Y.-N., et al. 2013, *MNRAS*, 433, 2946
- Wen, X.-Q., Wu, H., Zhu, Y.-N., et al. 2014, *MNRAS*, 438, 97
- West, A. A., Garcia-Appadoo, D. A., Dalcanton, J. J., et al. 2010, *AJ*, 139, 315
- Wright, E. L., Eisenhardt, P. R. M., Mainzer, A. K., et al. 2010, *AJ*, 140, 1868
- York, D. G., Adelman, J., Anderson, J. E., Jr., et al. 2000, *AJ*, 120, 1579
- Zhang, W., Li, C., Kauffmann, G., et al. 2009, *MNRAS*, 397, 1243
- Zhou, X., Fan, X.-H., Fan, Z., et al. 2016, *Research in Astronomy and Astrophysics*, 16, 69
- Zhou, Z.-M., Cao, C., & Wu, H. 2015, *AJ*, 149, 1
- Zhou, Z.-M., Zhou, X., Wu, H., et al. 2017, *ApJ*, 835, 70
- Zhu, Y.-N., Wu, H., Cao, C., & Li, H.-N. 2008, *ApJ*, 686, 155
- Zou, H., Jiang, Z., Zhou, X., et al. 2015, *AJ*, 150, 104

APPENDIX

A. THE ATLAS

An Atlas of the 70 galaxies in our sample is given in this Appendix. Table A.1 provides the information of the galaxies and the fluxes of H α and WISE IR emission. Table A.2 gives the physical properties and morphological parameters for galaxies. Figure A.1 displayed the images in broadband R , continuum-subtracted narrowband H α , WISE IR $3.4\mu\text{m}$ and $12\mu\text{m}$, along with the H α Spectrum from ALFALFA.

Table A.1. observational data of the target galaxies.

AGC	R.A.	Decl.	cz	Distance	S_{21}	$\log_{10}F_{3.4\mu\text{m}}$	$\log_{10}F_{12\mu\text{m}}$	$\log_{10}F_{H\alpha}$
	(deg)	(deg)	(km s $^{-1}$)	(Mpc)	(km s $^{-1}$)	(erg s $^{-1}$ cm $^{-2}$)	(erg s $^{-1}$ cm $^{-2}$)	(erg s $^{-1}$ cm $^{-2}$)
(1)	(2)	(3)	(4)	(5)	(6)	(7)	(8)	(9)
200803	165.04793	10.36444	11018	162.4 \pm 10.9	1.18 \pm 0.18	-11.88 \pm 0.01	-11.79 \pm 0.01	-13.40 \pm 0.03
200805	165.09541	9.84944	9296	137.8 \pm 9.3	1.31 \pm 0.15	-12.50 \pm 0.01	-12.84 \pm 0.12	-13.54 \pm 0.03
200845	165.48582	10.29500	10417	153.8 \pm 10.4	1.89 \pm 0.24	-11.93 \pm 0.01	-11.97 \pm 0.01	-12.99 \pm 0.03
200847	165.51083	10.34417	10721	158.2 \pm 10.8	0.78 \pm 0.11	-12.29 \pm 0.01	-12.44 \pm 0.05	-13.26 \pm 0.04
200855	165.59958	10.34333	11327	166.8 \pm 11.2	1.41 \pm 0.20	-12.29 \pm 0.01	-12.32 \pm 0.04	-13.66 \pm 0.03
200858	165.62459	9.98861	10682	157.6 \pm 10.6	0.74 \pm 0.14	-12.47 \pm 0.01	-12.54 \pm 0.07	-13.59 \pm 0.02
210063	166.95834	10.81361	9089	134.9 \pm 9.1	0.50 \pm 0.12	-12.03 \pm 0.01	-12.07 \pm 0.03	-13.51 \pm 0.02
210072	167.08084	10.0525	12255	180.1 \pm 12.1	2.14 \pm 0.21	-11.44 \pm 0.01	-11.56 \pm 0.01	-13.43 \pm 0.03
210073	167.07916	9.95694	12067	177.4 \pm 12.0	2.11 \pm 0.20	-11.58 \pm 0.01	-11.45 \pm 0.01	-13.20 \pm 0.01
210082	167.35042	10.83667	1555	17.5 \pm 1.4	2.72 \pm 0.10	-12.31 \pm 0.01	-12.68 \pm 0.08	-13.32 \pm 0.02
210084	167.35791	9.76972	7862	117.4 \pm 7.9	1.57 \pm 0.15	-12.00 \pm 0.01	-12.25 \pm 0.02	-13.87 \pm 0.04
210111	167.60583	10.12278	1320	17.5 \pm 1.2	3.02 \pm 0.13	-12.70 \pm 0.01	-12.55 \pm 0.06	-13.88 \pm 0.03
210148	167.91417	9.69444	13847	202.9 \pm 13.6	0.69 \pm 0.10	-12.18 \pm 0.01	-12.23 \pm 0.03	-13.79 \pm 0.10
210171	168.36581	10.48472	8885	131.9 \pm 8.8	1.16 \pm 0.13	-11.55 \pm 0.01	-12.04 \pm 0.02	-13.39 \pm 0.02
210180	168.68459	10.22833	13958	204.4 \pm 13.7	1.34 \pm 0.18	-11.71 \pm 0.01	-11.64 \pm 0.01	-13.47 \pm 0.02
210354	172.06084	9.08278	6254	94.4 \pm 6.3	4.58 \pm 0.17	-11.51 \pm 0.01	-11.40 \pm 0.01	-12.70 \pm 0.00
210368	172.25792	9.10083	6287	94.9 \pm 6.4	1.55 \pm 0.11	-12.37 \pm 0.01	-12.64 \pm 0.08	-13.76 \pm 0.04
211086	167.12582	10.80806	10978	161.8 \pm 10.9	1.07 \pm 0.17	-12.15 \pm 0.01	-12.16 \pm 0.03	-13.79 \pm 0.03
212984	165.99001	10.10806	9907	146.6 \pm 9.8	1.21 \pm 0.14	-12.00 \pm 0.01	-12.02 \pm 0.02	-14.24 \pm 0.10
212987	166.30249	10.44778	9220	136.7 \pm 9.3	1.34 \pm 0.12	-12.60 \pm 0.01	-12.90 \pm 0.12	-13.46 \pm 0.05
212988	166.53793	10.03222	5776	87.5 \pm 6.0	0.40 \pm 0.11	-12.63 \pm 0.01	-12.98 \pm 0.14	-14.29 \pm 0.06
212989	166.53625	10.14528	14349	210.0 \pm 14.1	0.64 \pm 0.13	-12.15 \pm 0.01	-12.32 \pm 0.04	-13.77 \pm 0.02
212990	166.79501	10.26639	9005	133.7 \pm 9.0	2.33 \pm 0.11	-12.43 \pm 0.01	-12.49 \pm 0.05	-13.89 \pm 0.08
212994	167.10957	10.48944	13805	202.2 \pm 13.6	0.53 \pm 0.12	-12.08 \pm 0.01	-12.24 \pm 0.03	-13.62 \pm 0.01
212996	167.46541	10.40083	8928	132.6 \pm 8.9	1.55 \pm 0.19	-12.33 \pm 0.02	-12.38 \pm 0.04	-13.90 \pm 0.02
213010	170.49083	10.49444	4461	66.2 \pm 4.8	0.96 \pm 0.10	-12.57 \pm 0.01	-13.05 \pm 4.34	-15.71 \pm 3.10
213058	165.63792	9.47194	8241	122.8 \pm 8.2	0.92 \pm 0.19	-11.70 \pm 0.01	-11.96 \pm 0.01	-13.54 \pm 0.01
213062	166.77167	9.80222	6254	94.4 \pm 6.3	0.88 \pm 0.06	-12.46 \pm 0.01	-12.59 \pm 0.07	-13.56 \pm 0.05
213064	167.72626	9.62278	1604	17.5 \pm 1.4	3.65 \pm 0.10	-12.01 \pm 0.01	-12.31 \pm 0.03	-12.68 \pm 0.01
213069	168.20749	9.52278	6250	94.3 \pm 6.3	1.10 \pm 0.11	-12.76 \pm 0.01	-12.85 \pm 0.36	-14.62 \pm 0.37
213072	169.71918	9.62889	9278	137.6 \pm 9.2	0.86 \pm 0.05	-11.96 \pm 0.01	-11.84 \pm 0.01	-13.46 \pm 0.01

Table A.1 continued

Table A.1 (continued)

AGC	R.A.	Decl.	cz	Distance	S_{21}	$\log_{10}F_{3.4\mu m}$	$\log_{10}F_{12\mu m}$	$\log_{10}F_{H\alpha}$
	(deg)	(deg)	(km s $^{-1}$)	(Mpc)	(km s $^{-1}$)	(erg s $^{-1}$ cm $^{-2}$)	(erg s $^{-1}$ cm $^{-2}$)	(erg s $^{-1}$ cm $^{-2}$)
(1)	(2)	(3)	(4)	(5)	(6)	(7)	(8)	(9)
213074	169.86583	9.59917	990	13.7 ± 0.9	2.14 ± 0.05	-13.00 ± 0.02	-13.13 ± 1.00	-13.40 ± 0.01
213076	170.32251	9.15194	8981	133.3 ± 8.9	1.55 ± 0.13	-12.39 ± 0.01	-12.59 ± 0.06	-14.15 ± 0.09
213083	170.86749	9.08750	9456	140.1 ± 9.4	0.61 ± 0.12	-12.43 ± 0.01	-12.64 ± 0.07	-14.39 ± 0.06
213085	171.63333	9.91945	9391	139.2 ± 9.3	1.22 ± 0.11	-12.74 ± 0.01	-12.84 ± 0.25	-14.20 ± 0.25
213087	172.05290	9.80417	9321	138.2 ± 9.4	1.31 ± 0.15	-12.15 ± 0.01	-12.39 ± 0.04	-13.90 ± 0.04
213090	172.36917	10.62361	5855	88.6 ± 5.9	0.98 ± 0.06	-12.70 ± 0.01	-12.79 ± 0.11	-13.43 ± 0.01
213092	172.41000	9.96444	5887	89.1 ± 6.2	1.51 ± 0.13	-12.14 ± 0.01	-12.12 ± 0.03	-13.63 ± 0.01
213198	168.51875	10.98972	12357	181.5 ± 12.2	0.61 ± 0.09	-12.10 ± 0.01	-12.34 ± 0.04	-13.40 ± 0.02
213573	165.16417	9.22806	10723	158.2 ± 10.6	0.97 ± 0.14	-12.48 ± 0.01	-12.67 ± 0.08	-13.75 ± 0.03
213574	165.16917	9.04778	10651	157.2 ± 10.6	0.28 ± 0.06	-12.14 ± 0.01	-12.38 ± 0.06	-14.16 ± 0.02
213583	165.39708	9.38944	11826	174.0 ± 11.7	0.73 ± 0.09	-12.09 ± 0.01	-12.05 ± 0.02	-13.32 ± 0.03
213586	165.97125	9.13944	12171	178.9 ± 12.0	0.63 ± 0.12	-11.41 ± 0.00	-12.73 ± 0.07	-13.85 ± 0.01
213588	166.53084	9.63806	12358	181.6 ± 12.2	0.79 ± 0.11	-12.78 ± 0.01	-12.88 ± 0.25	-13.45 ± 0.09
213590	167.12709	9.92556	12027	176.8 ± 11.9	1.67 ± 0.17	-12.50 ± 0.01	-12.52 ± 0.05	-13.36 ± 0.01
213596	167.57959	9.50917	13260	194.5 ± 13.1	1.00 ± 0.15	-12.14 ± 0.01	-12.16 ± 0.02	-14.57 ± 0.22
213603	167.99208	9.46028	14080	206.2 ± 13.8	0.34 ± 0.06	-12.67 ± 0.01	-13.06 ± 0.20	-14.15 ± 0.02
213609	168.20876	9.73389	14033	205.5 ± 13.8	1.01 ± 0.15	-12.27 ± 0.01	-12.40 ± 0.05	-13.73 ± 0.01
213611	168.47542	9.64583	12370	181.8 ± 12.2	1.14 ± 0.10	-11.65 ± 0.00	-12.19 ± 0.02	-13.38 ± 0.02
215236	166.10249	10.26389	9314	138.1 ± 9.3	1.29 ± 0.16	-12.99 ± 0.02	-13.03 ± 0.21	-13.98 ± 0.04
215237	166.35249	10.67500	9233	136.9 ± 9.2	0.84 ± 0.14	-13.18 ± 0.03	-13.03 ± 0.17	-13.78 ± 0.08
215239	167.27249	10.16722	11916	175.3 ± 11.7	1.01 ± 0.11	-13.16 ± 0.03	-13.11 ± 0.86	-13.87 ± 0.04
215240	168.47542	9.93583	1610	17.5 ± 1.4	0.46 ± 0.06	-13.20 ± 0.03	-13.07 ± 1.00	-15.39 ± 1.97
215241	169.25917	10.14778	1765	17.5 ± 1.8	1.97 ± 0.11	-12.97 ± 0.02	-13.09 ± 2.10	-15.05 ± 1.17
215242	167.09500	10.08333	9090	134.9 ± 9.1	0.78 ± 0.11	-13.07 ± 0.02	-12.83 ± 0.24	-14.37 ± 0.18
215761	165.64250	9.48167	10486	154.8 ± 10.4	1.36 ± 0.16	-12.35 ± 0.01	-12.55 ± 0.05	-13.27 ± 0.01
219116	165.89792	9.29194	8226	122.6 ± 8.2	0.93 ± 0.10	-13.11 ± 0.03	-12.93 ± 0.54	-13.65 ± 0.02
6086	165.14334	9.95333	9304	137.9 ± 9.3	2.40 ± 0.31	-11.85 ± 0.01	-12.09 ± 0.02	-13.41 ± 0.03
6091	165.16708	9.87639	10715	158.1 ± 10.6	3.49 ± 0.20	-11.51 ± 0.01	-11.86 ± 0.01	-13.02 ± 0.01
6093	165.20375	10.73056	10806	159.4 ± 10.8	1.36 ± 0.15	-11.29 ± 0.01	-12.05 ± 0.02	-12.87 ± 0.01
6209	167.48624	10.72000	1584	18.1 ± 1.4	8.58 ± 0.25	-11.25 ± 0.01	-11.16 ± 0.00	-11.95 ± 0.01
6245	168.17125	9.06528	1421	17.5 ± 1.2	1.39 ± 0.12	-10.79 ± 0.01	-10.45 ± 0.00	-12.37 ± 0.01
6248	168.21750	10.19972	1286	17.5 ± 1.1	2.53 ± 0.05	-12.86 ± 0.02	-13.08 ± 0.19	-13.65 ± 0.05
6288	169.01500	10.17083	5897	89.3 ± 6.0	2.46 ± 0.14	-12.15 ± 0.01	-12.37 ± 0.04	-13.29 ± 0.01
6438	171.47292	9.98472	1156	20.4 ± 1.5	3.88 ± 0.07	-11.47 ± 0.01	-11.87 ± 0.01	-13.54 ± 0.01
6470	172.05916	9.14778	6311	95.2 ± 6.4	5.77 ± 0.20	-10.99 ± 0.01	-10.88 ± 0.00	-12.58 ± 0.01
6474	172.09750	9.41083	1716	33.1 ± 2.1	12.37 ± 0.21	-10.76 ± 0.01	-11.43 ± 0.00	-12.28 ± 0.01
6475	172.14458	9.09805	6309	95.2 ± 6.5	7.40 ± 0.22	-11.16 ± 0.01	-11.43 ± 0.00	-12.99 ± 0.01
6477	172.15457	9.09972	6288	94.9 ± 6.5	5.63 ± 0.13	-11.55 ± 0.01	-11.57 ± 0.01	-12.60 ± 0.01
6482	172.26625	9.10639	6201	93.6 ± 6.3	2.03 ± 0.22	-10.69 ± 0.01	-10.40 ± 0.00	-12.58 ± 0.01

Table A.2. Physical properties of the target galaxies.

AGC	$\log_{10} M_{\text{HI}}$	$\log_{10} M_*$	$\log_{10} \text{SFR}$	C_R	A_R	S_R	$C_{\text{H}\alpha}$	$A_{\text{H}\alpha}$	$S_{\text{H}\alpha}$
	(M_{\odot})	(M_{\odot})	($M_{\odot} \text{ yr}^{-1}$)						
(1)	(2)	(3)	(4)	(5)	(6)	(7)	(8)	(9)	(10)
200803	9.87 ± 0.07	10.07 ± 0.01	0.03 ± 0.01	2.36 ± 0.02	0.35 ± 0.01	0.75 ± 0.02	2.84 ± 0.11	0.30 ± 0.14	2.72 ± 0.16
200805	9.77 ± 0.05	9.22 ± 0.02	-1.08 ± 0.10	2.67 ± 0.05	0.17 ± 0.03	0.58 ± 0.03	1.80 ± 0.10	0.46 ± 0.13	1.70 ± 0.15
200845	10.02 ± 0.05	9.97 ± 0.01	-0.19 ± 0.02	2.70 ± 0.05	0.13 ± 0.03	0.73 ± 0.03	3.39 ± 0.11	0.53 ± 0.14	2.44 ± 0.16
200847	9.66 ± 0.06	9.59 ± 0.01	-0.62 ± 0.05	1.88 ± 0.08	0.64 ± 0.05	1.51 ± 0.05	1.29 ± 0.16	0.49 ± 0.20	2.26 ± 0.23
200855	9.97 ± 0.06	9.64 ± 0.02	-0.45 ± 0.04	2.62 ± 0.02	0.18 ± 0.01	0.51 ± 0.01	2.64 ± 0.11	0.59 ± 0.14	2.23 ± 0.16
200858	9.64 ± 0.08	9.39 ± 0.02	-0.24 ± 0.03	2.49 ± 0.03	0.17 ± 0.02	0.95 ± 0.02	1.76 ± 0.10	0.42 ± 0.12	1.71 ± 0.13
210063	9.33 ± 0.10	9.73 ± 0.02	-0.18 ± 0.02	2.29 ± 0.01	0.19 ± 0.01	0.65 ± 0.01	1.46 ± 0.09	0.65 ± 0.12	1.84 ± 0.13
210072	10.21 ± 0.04	10.67 ± 0.01	0.43 ± 0.01	2.66 ± 0.01	0.15 ± 0.01	0.56 ± 0.01	2.96 ± 0.11	0.58 ± 0.13	2.12 ± 0.15
210073	10.19 ± 0.04	10.50 ± 0.01	0.44 ± 0.01	2.88 ± 0.02	0.15 ± 0.01	0.60 ± 0.01	2.47 ± 0.04	0.44 ± 0.04	1.79 ± 0.05
210082	8.29 ± 0.02	7.43 ± 0.01	-2.49 ± 0.04	2.20 ± 0.01	0.13 ± 0.00	0.39 ± 0.01	1.19 ± 0.09	0.55 ± 0.11	3.16 ± 0.13
210084	9.71 ± 0.04	9.62 ± 0.01	-0.48 ± 0.02	2.20 ± 0.01	0.19 ± 0.01	0.78 ± 0.01	2.45 ± 0.15	0.05 ± 0.18	0.36 ± 0.21
210111	8.34 ± 0.02	6.99 ± 0.01	-2.27 ± 0.04	2.38 ± 0.02	0.35 ± 0.01	0.71 ± 0.01	2.17 ± 0.13	0.51 ± 0.16	1.05 ± 0.18
210148	9.83 ± 0.07	9.95 ± 0.01	-0.22 ± 0.03	2.60 ± 0.03	0.24 ± 0.02	0.83 ± 0.02	1.86 ± 0.33	0.46 ± 0.41	3.62 ± 0.47
210171	9.68 ± 0.05	10.24 ± 0.01	-0.38 ± 0.02	2.61 ± 0.01	0.10 ± 0.00	0.17 ± 0.01	1.90 ± 0.08	0.43 ± 0.10	2.10 ± 0.12
210180	10.12 ± 0.06	10.48 ± 0.01	0.38 ± 0.01	2.52 ± 0.02	0.22 ± 0.01	0.21 ± 0.01	2.20 ± 0.08	0.60 ± 0.10	2.49 ± 0.12
210354	9.98 ± 0.02	9.96 ± 0.01	-0.04 ± 0.01	2.51 ± 0.01	0.11 ± 0.01	0.36 ± 0.01	2.12 ± 0.02	0.33 ± 0.03	1.04 ± 0.03
210368	9.52 ± 0.03	9.01 ± 0.01	-0.74 ± 0.04	2.61 ± 0.03	0.31 ± 0.01	0.53 ± 0.02	4.08 ± 0.14	0.56 ± 0.18	1.90 ± 0.20
211086	9.82 ± 0.07	9.77 ± 0.01	-0.34 ± 0.03	2.92 ± 0.02	0.10 ± 0.01	0.61 ± 0.02	2.85 ± 0.13	0.48 ± 0.16	2.27 ± 0.18
212984	9.79 ± 0.05	9.83 ± 0.01	-0.21 ± 0.03	2.76 ± 0.02	0.18 ± 0.01	0.21 ± 0.02	1.24 ± 0.34	0.01 ± 0.42	0.12 ± 0.48
212987	9.77 ± 0.04	9.10 ± 0.02	-1.06 ± 0.08	2.68 ± 0.06	0.32 ± 0.03	1.33 ± 0.04	2.41 ± 0.18	0.50 ± 0.22	2.82 ± 0.25
212988	8.86 ± 0.12	8.63 ± 0.02	-1.3 ± 0.07	3.30 ± 0.04	0.26 ± 0.02	1.22 ± 0.02	1.92 ± 0.23	0.45 ± 0.28	2.80 ± 0.32
212989	9.82 ± 0.09	10.02 ± 0.02	0.00 ± 0.02	2.37 ± 0.02	0.35 ± 0.01	0.33 ± 0.01	2.21 ± 0.07	0.58 ± 0.09	2.03 ± 0.11
212990	9.99 ± 0.02	9.26 ± 0.02	-0.82 ± 0.05	2.51 ± 0.03	0.25 ± 0.02	0.65 ± 0.02	1.85 ± 0.29	0.54 ± 0.36	0.67 ± 0.41
212994	9.71 ± 0.10	10.07 ± 0.01	0.10 ± 0.02	2.66 ± 0.01	0.14 ± 0.01	0.26 ± 0.01	2.10 ± 0.05	0.48 ± 0.07	2.27 ± 0.08
212996	9.81 ± 0.06	9.37 ± 0.02	-0.45 ± 0.02	2.88 ± 0.02	0.32 ± 0.01	0.53 ± 0.01	2.48 ± 0.07	0.37 ± 0.08	1.60 ± 0.09
213010	9.00 ± 0.04	8.43 ± 0.02	-2.03 ± 0.32	2.27 ± 0.03	0.28 ± 0.02	0.42 ± 0.02	1.47 ± 0.31	0.44 ± 0.44	2.98 ± 0.42
213058	9.51 ± 0.09	10.01 ± 0.01	-0.15 ± 0.01	2.65 ± 0.01	0.16 ± 0.01	0.21 ± 0.01	2.10 ± 0.04	0.52 ± 0.05	2.01 ± 0.06
213062	9.27 ± 0.03	8.89 ± 0.01	-1.17 ± 0.06	2.74 ± 0.04	0.40 ± 0.02	1.20 ± 0.02	2.55 ± 0.17	0.55 ± 0.21	1.16 ± 0.24
213064	8.42 ± 0.01	7.76 ± 0.01	-1.93 ± 0.01	2.82 ± 0.01	0.30 ± 0.01	0.08 ± 0.01	2.84 ± 0.01	0.40 ± 0.01	0.19 ± 0.01
213069	9.36 ± 0.04	8.56 ± 0.02	-1.50 ± 0.35	2.64 ± 0.04	0.14 ± 0.02	0.58 ± 0.02	1.62 ± 0.31	0.69 ± 0.48	3.88 ± 0.41
213072	9.58 ± 0.03	9.82 ± 0.01	-0.16 ± 0.01	2.29 ± 0.02	0.09 ± 0.01	0.39 ± 0.01	2.23 ± 0.06	0.61 ± 0.07	2.22 ± 0.09
213074	7.98 ± 0.01	6.42 ± 0.03	-2.33 ± 0.08	3.56 ± 0.04	0.54 ± 0.02	0.94 ± 0.03	2.29 ± 0.06	0.50 ± 0.08	2.10 ± 0.09
213076	9.81 ± 0.04	9.31 ± 0.01	-0.93 ± 0.06	2.42 ± 0.03	0.03 ± 0.01	0.52 ± 0.02	2.22 ± 0.31	0.33 ± 0.38	2.97 ± 0.44
213083	9.45 ± 0.08	9.31 ± 0.01	-0.76 ± 0.05	2.60 ± 0.03	0.22 ± 0.02	0.24 ± 0.02	2.45 ± 0.22	0.64 ± 0.27	2.21 ± 0.31
213085	9.75 ± 0.04	8.96 ± 0.02	-1.14 ± 0.24	2.72 ± 0.03	0.34 ± 0.02	1.30 ± 0.02	0.93 ± 0.34	0.47 ± 0.42	3.44 ± 0.28
213087	9.77 ± 0.05	9.62 ± 0.01	-0.53 ± 0.04	3.29 ± 0.03	0.20 ± 0.02	0.42 ± 0.02	4.43 ± 0.15	0.40 ± 0.18	2.54 ± 0.21

Table A.2 continued

Table A.2 (continued)

AGC	$\log_{10} M_{\text{HI}}$	$\log_{10} M_*$	$\log_{10} \text{SFR}$	C_R	A_R	S_R	$C_{\text{H}\alpha}$	$A_{\text{H}\alpha}$	$S_{\text{H}\alpha}$
	(M_{\odot})	(M_{\odot})	($M_{\odot} \text{ yr}^{-1}$)						
(1)	(2)	(3)	(4)	(5)	(6)	(7)	(8)	(9)	(10)
213090	9.26 ± 0.03	8.56 ± 0.02	-0.71 ± 0.02	1.99 ± 0.02	0.68 ± 0.01	0.92 ± 0.01	1.17 ± 0.03	0.90 ± 0.04	1.53 ± 0.05
213092	9.45 ± 0.04	9.20 ± 0.02	-0.60 ± 0.02	2.56 ± 0.01	0.38 ± 0.01	0.28 ± 0.01	2.21 ± 0.03	0.55 ± 0.04	1.46 ± 0.04
213198	9.68 ± 0.07	9.94 ± 0.01	-0.38 ± 0.04	2.26 ± 0.03	0.20 ± 0.02	0.66 ± 0.02	1.85 ± 0.07	0.53 ± 0.08	2.29 ± 0.10
213573	9.76 ± 0.07	9.38 ± 0.02	-0.83 ± 0.08	2.80 ± 0.04	0.12 ± 0.02	0.65 ± 0.03	2.64 ± 0.13	0.55 ± 0.15	0.50 ± 0.18
213574	9.21 ± 0.10	9.75 ± 0.01	-0.44 ± 0.04	3.04 ± 0.02	0.19 ± 0.01	0.48 ± 0.01	2.38 ± 0.09	0.42 ± 0.11	1.90 ± 0.13
213583	9.72 ± 0.06	9.90 ± 0.01	-0.16 ± 0.03	2.58 ± 0.06	0.19 ± 0.03	0.90 ± 0.04	2.70 ± 0.10	0.28 ± 0.12	2.21 ± 0.14
213586	9.68 ± 0.08	10.69 ± 0.01	-0.39 ± 0.03	3.68 ± 0.01	0.17 ± 0.01	0.35 ± 0.01	4.41 ± 0.05	0.09 ± 0.06	0.06 ± 0.06
213588	9.79 ± 0.07	9.18 ± 0.02	-0.77 ± 0.16	2.92 ± 0.06	0.38 ± 0.03	0.81 ± 0.04	2.63 ± 0.29	0.29 ± 0.36	1.58 ± 0.41
213590	10.09 ± 0.04	9.46 ± 0.02	-0.53 ± 0.04	2.01 ± 0.02	0.43 ± 0.01	0.38 ± 0.02	1.56 ± 0.05	0.01 ± 0.06	1.00 ± 0.06
213596	9.95 ± 0.07	9.95 ± 0.01	-0.19 ± 0.03	2.63 ± 0.02	0.11 ± 0.01	0.23 ± 0.01	2.02 ± 0.73	0.58 ± 0.40	3.56 ± 0.44
213603	9.53 ± 0.09	9.42 ± 0.02	-0.47 ± 0.06	2.69 ± 0.04	0.43 ± 0.02	0.55 ± 0.03	2.48 ± 0.09	0.42 ± 0.11	1.42 ± 0.12
213609	10.00 ± 0.06	9.86 ± 0.02	-0.02 ± 0.03	2.67 ± 0.02	0.14 ± 0.01	0.21 ± 0.01	2.55 ± 0.06	0.27 ± 0.08	1.60 ± 0.09
213611	9.95 ± 0.04	10.44 ± 0.01	-0.23 ± 0.02	3.18 ± 0.02	0.08 ± 0.01	0.28 ± 0.01	3.72 ± 0.07	0.41 ± 0.09	2.00 ± 0.10
215236	9.76 ± 0.06	8.67 ± 0.03	-1.23 ± 0.18	2.27 ± 0.15	0.05 ± 0.08	1.15 ± 0.09	2.19 ± 0.16	0.64 ± 0.20	2.73 ± 0.23
215237	9.57 ± 0.07	8.45 ± 0.04	-1.24 ± 0.13	2.64 ± 0.17	0.26 ± 0.10	2.07 ± 0.11	1.44 ± 0.28	0.04 ± 0.35	0.53 ± 0.40
215239	9.86 ± 0.05	8.71 ± 0.04	-1.05 ± 0.56	2.36 ± 0.09	0.34 ± 0.05	0.81 ± 0.06	1.89 ± 0.13	0.03 ± 0.16	0.24 ± 0.19
215240	7.52 ± 0.06	6.43 ± 0.04	-3.18 ± 1.03	2.33 ± 0.10	0.30 ± 0.06	0.67 ± 0.06	1.74 ± 0.56	0.13 ± 0.64	2.58 ± 0.38
215241	8.15 ± 0.03	6.68 ± 0.03	-3.16 ± 1.92	2.61 ± 0.05	0.28 ± 0.03	0.64 ± 0.03	0.34 ± 0.41	0.48 ± 0.57	2.56 ± 0.31
215242	9.52 ± 0.06	8.56 ± 0.03	-1.16 ± 0.23	2.85 ± 0.09	0.45 ± 0.05	1.25 ± 0.06	1.79 ± 0.31	0.57 ± 0.54	3.04 ± 0.36
215761	9.89 ± 0.05	9.50 ± 0.01	-0.66 ± 0.04	2.90 ± 0.02	0.24 ± 0.01	0.14 ± 0.02	3.30 ± 0.04	0.45 ± 0.05	0.99 ± 0.06
219116	9.52 ± 0.05	8.42 ± 0.03	-0.34 ± 0.06	2.31 ± 0.16	0.49 ± 0.09	1.45 ± 0.10	2.11 ± 0.08	0.58 ± 0.10	2.37 ± 0.12
6086	10.03 ± 0.06	9.95 ± 0.01	-0.40 ± 0.02	3.22 ± 0.02	0.24 ± 0.01	0.69 ± 0.02	1.92 ± 0.12	0.61 ± 0.14	2.56 ± 0.17
6091	10.31 ± 0.03	10.46 ± 0.01	0.08 ± 0.01	3.86 ± 0.01	0.32 ± 0.01	0.53 ± 0.01	2.76 ± 0.02	0.53 ± 0.02	1.63 ± 0.02
6093	9.91 ± 0.05	10.71 ± 0.01	-0.17 ± 0.02	3.37 ± 0.01	0.17 ± 0.01	0.52 ± 0.01	2.08 ± 0.06	0.42 ± 0.07	0.25 ± 0.08
6209	8.82 ± 0.01	8.64 ± 0.01	-1.01 ± 0.01	2.61 ± 0.01	0.19 ± 0.00	0.44 ± 0.00	2.52 ± 0.01	0.79 ± 0.00	1.29 ± 0.01
6245	8.00 ± 0.04	9.13 ± 0.01	-0.56 ± 0.01	3.27 ± 0.01	0.22 ± 0.00	0.30 ± 0.00	2.07 ± 0.01	0.89 ± 0.01	1.92 ± 0.01
6248	8.26 ± 0.01	6.80 ± 0.02	-2.02 ± 0.06	2.73 ± 0.04	0.36 ± 0.02	0.19 ± 0.03	1.93 ± 0.19	0.51 ± 0.24	2.94 ± 0.27
6288	9.66 ± 0.03	9.19 ± 0.01	-0.83 ± 0.02	2.60 ± 0.01	0.12 ± 0.01	0.07 ± 0.01	2.14 ± 0.02	0.37 ± 0.02	0.85 ± 0.03
6438	8.58 ± 0.01	8.52 ± 0.01	-1.78 ± 0.01	3.24 ± 0.01	0.13 ± 0.01	0.04 ± 0.01	1.32 ± 0.05	0.99 ± 0.07	2.38 ± 0.08
6470	10.09 ± 0.02	10.55 ± 0.01	0.60 ± 0.01	3.20 ± 0.01	0.37 ± 0.01	0.44 ± 0.01	3.52 ± 0.01	0.58 ± 0.02	1.09 ± 0.02
6474	9.50 ± 0.01	9.78 ± 0.01	-0.84 ± 0.01	3.68 ± 0.01	0.15 ± 0.00	0.95 ± 0.00	3.23 ± 0.01	0.34 ± 0.01	1.36 ± 0.01
6475	10.20 ± 0.01	10.36 ± 0.01	-0.01 ± 0.01	3.52 ± 0.01	0.16 ± 0.01	1.59 ± 0.01	3.09 ± 0.01	0.52 ± 0.02	2.02 ± 0.02
6477	10.08 ± 0.01	9.92 ± 0.01	-0.02 ± 0.01	2.61 ± 0.01	0.26 ± 0.00	0.23 ± 0.01	1.99 ± 0.01	0.61 ± 0.01	1.32 ± 0.01
6482	9.62 ± 0.05	10.87 ± 0.01	0.95 ± 0.01	3.20 ± 0.01	0.25 ± 0.01	0.35 ± 0.00	1.98 ± 0.01	0.47 ± 0.01	0.95 ± 0.01

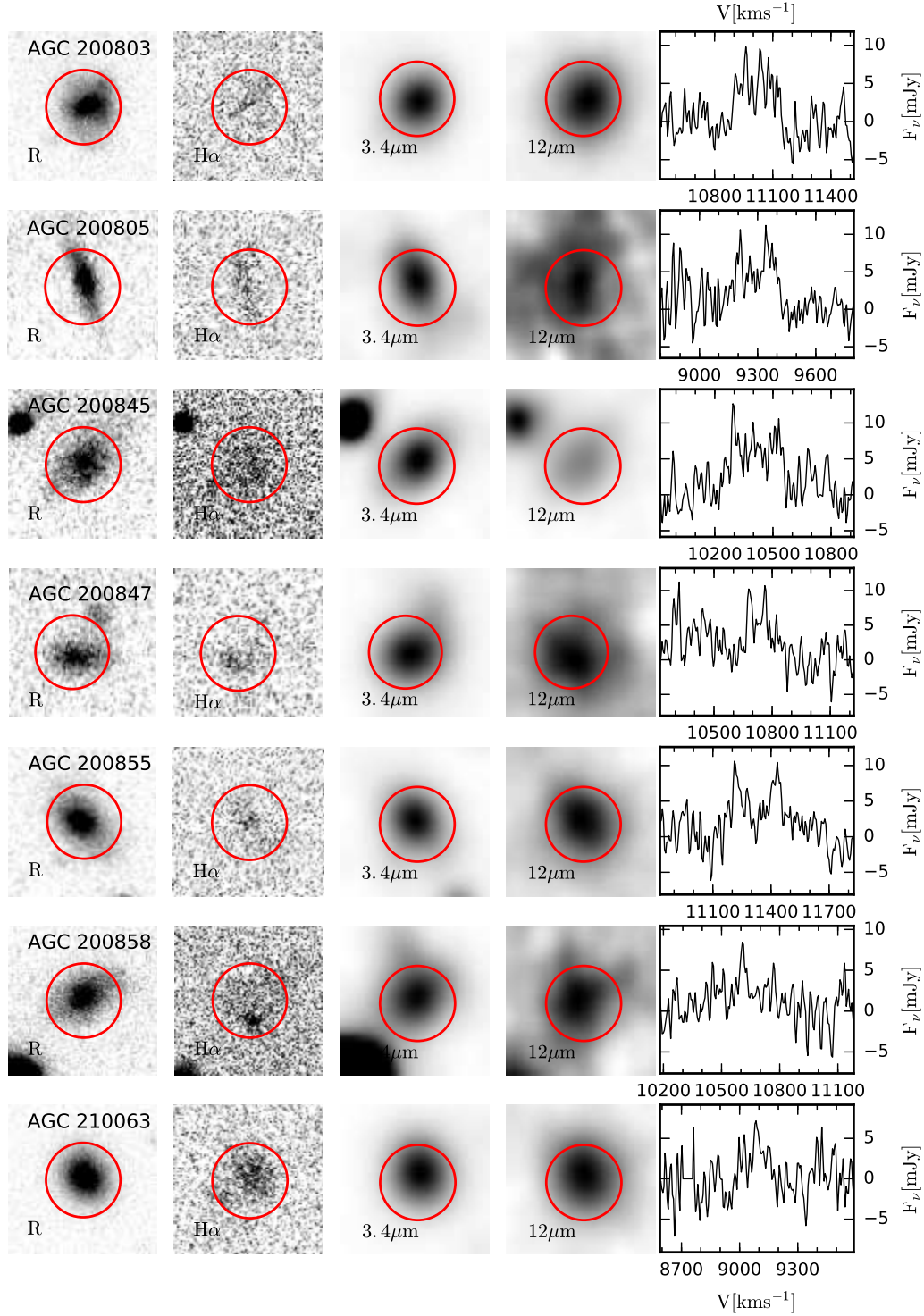


Figure A.1. Images in broadband R , continuum-subtracted narrowband $H\alpha$, WISE IR $3.4\mu\text{m}$ and $12\mu\text{m}$, along with the Global HI profiles from ALFALFA for all 70 targets. Petrosian radii of SDSS r band are overlaid on the images.

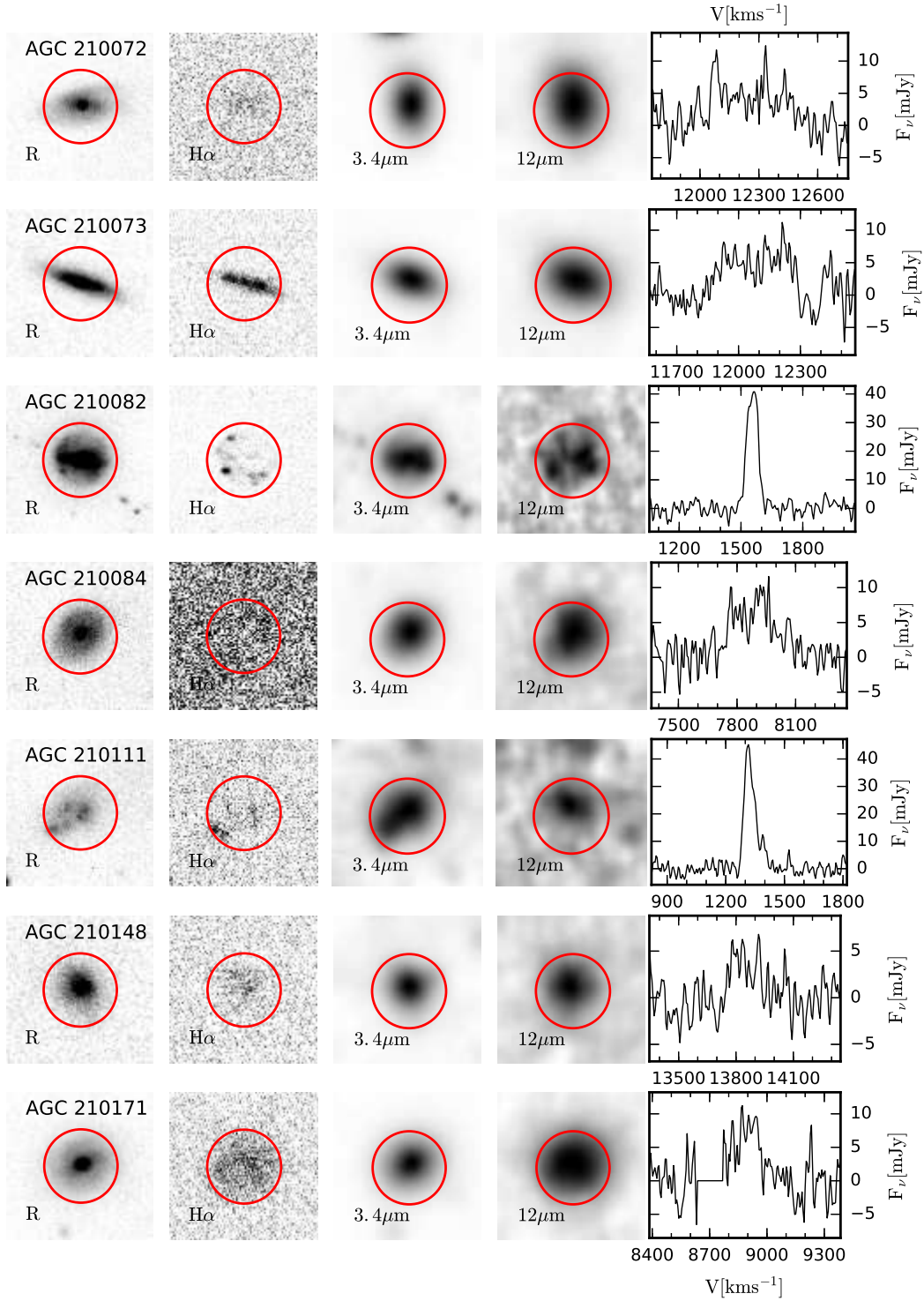


Figure A.1. (Continued)

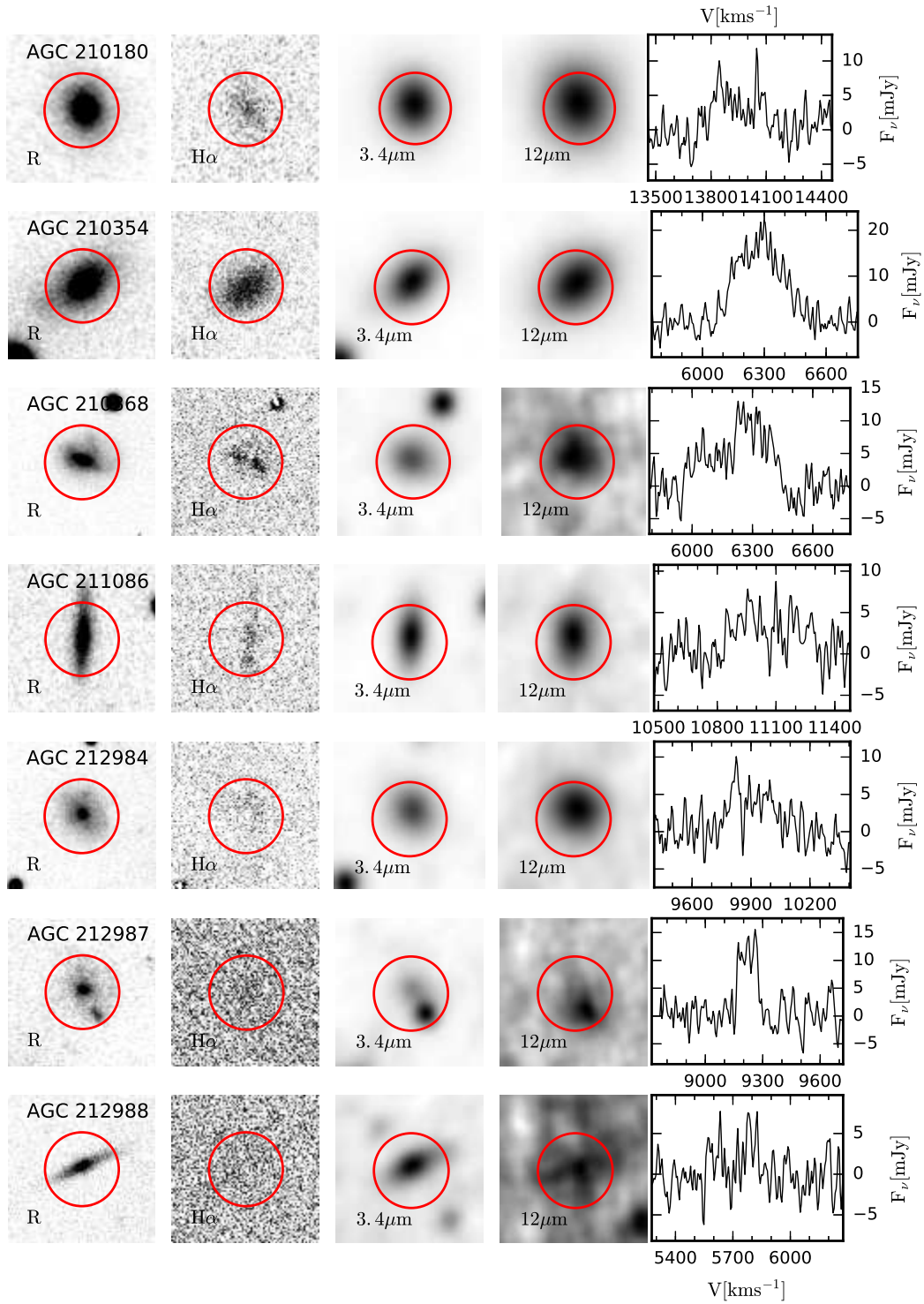


Figure A.1. (Continued)

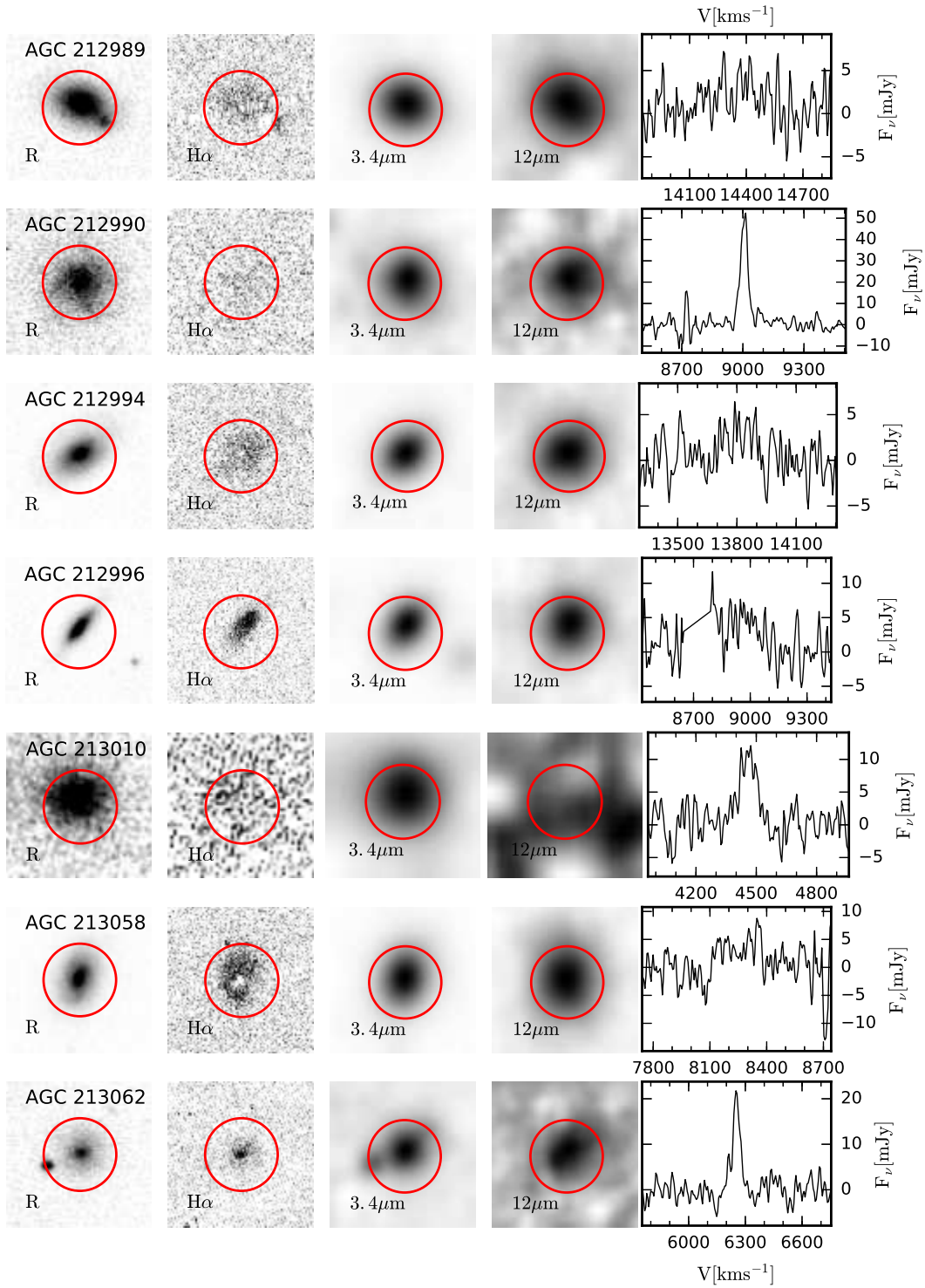


Figure A.1. (Continued)

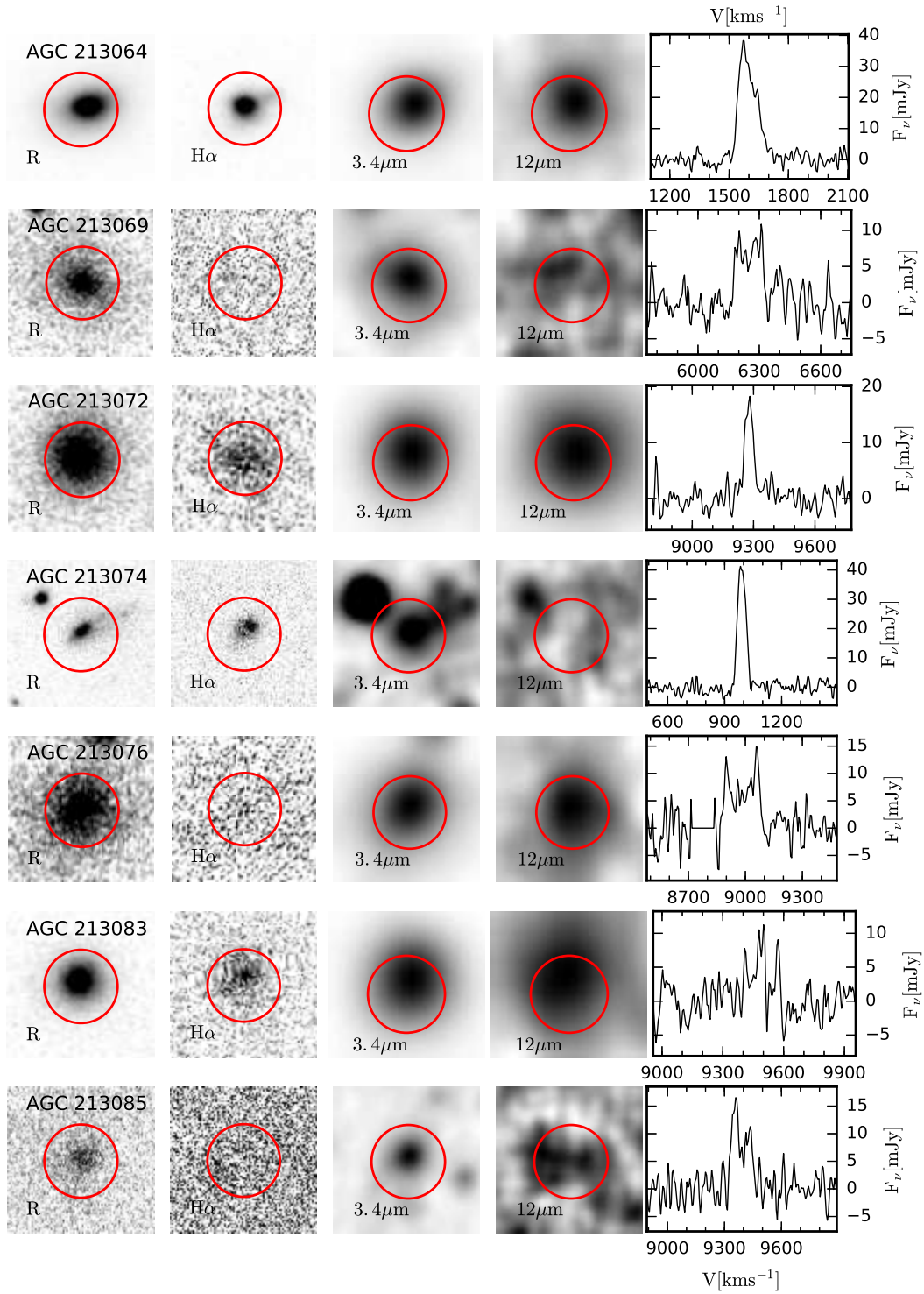


Figure A.1. (Continued)

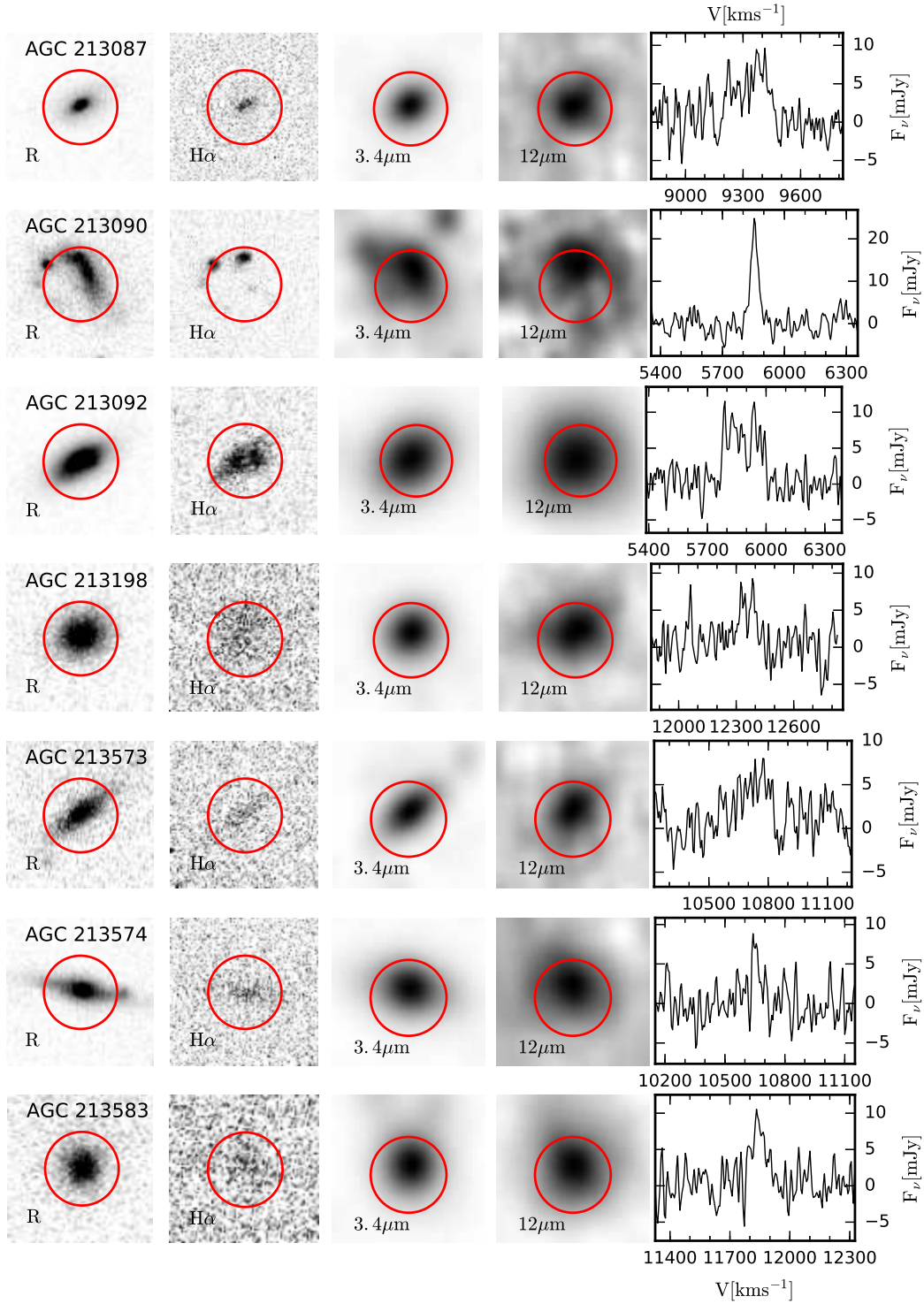


Figure A.1. (Continued)

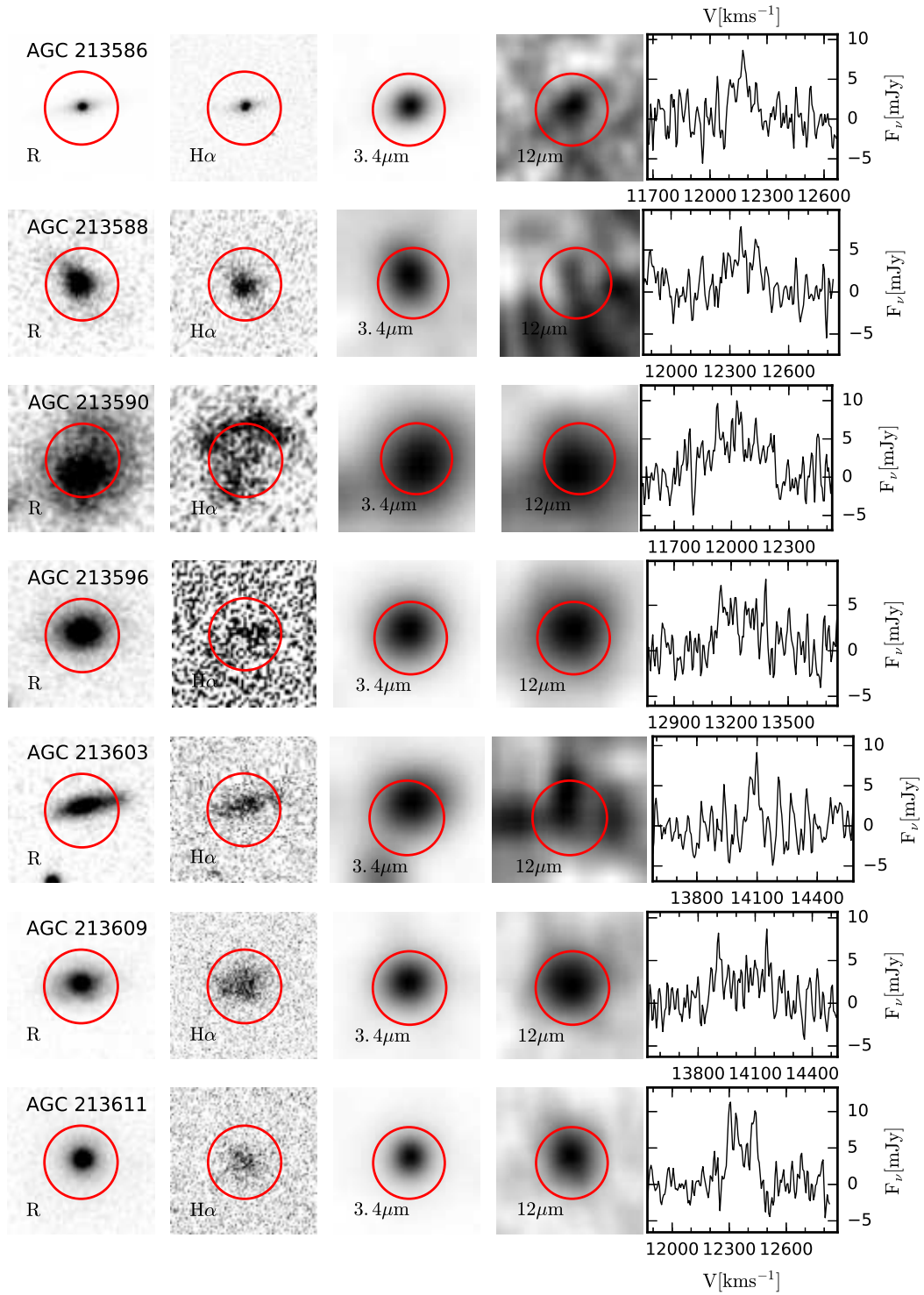


Figure A.1. (Continued)

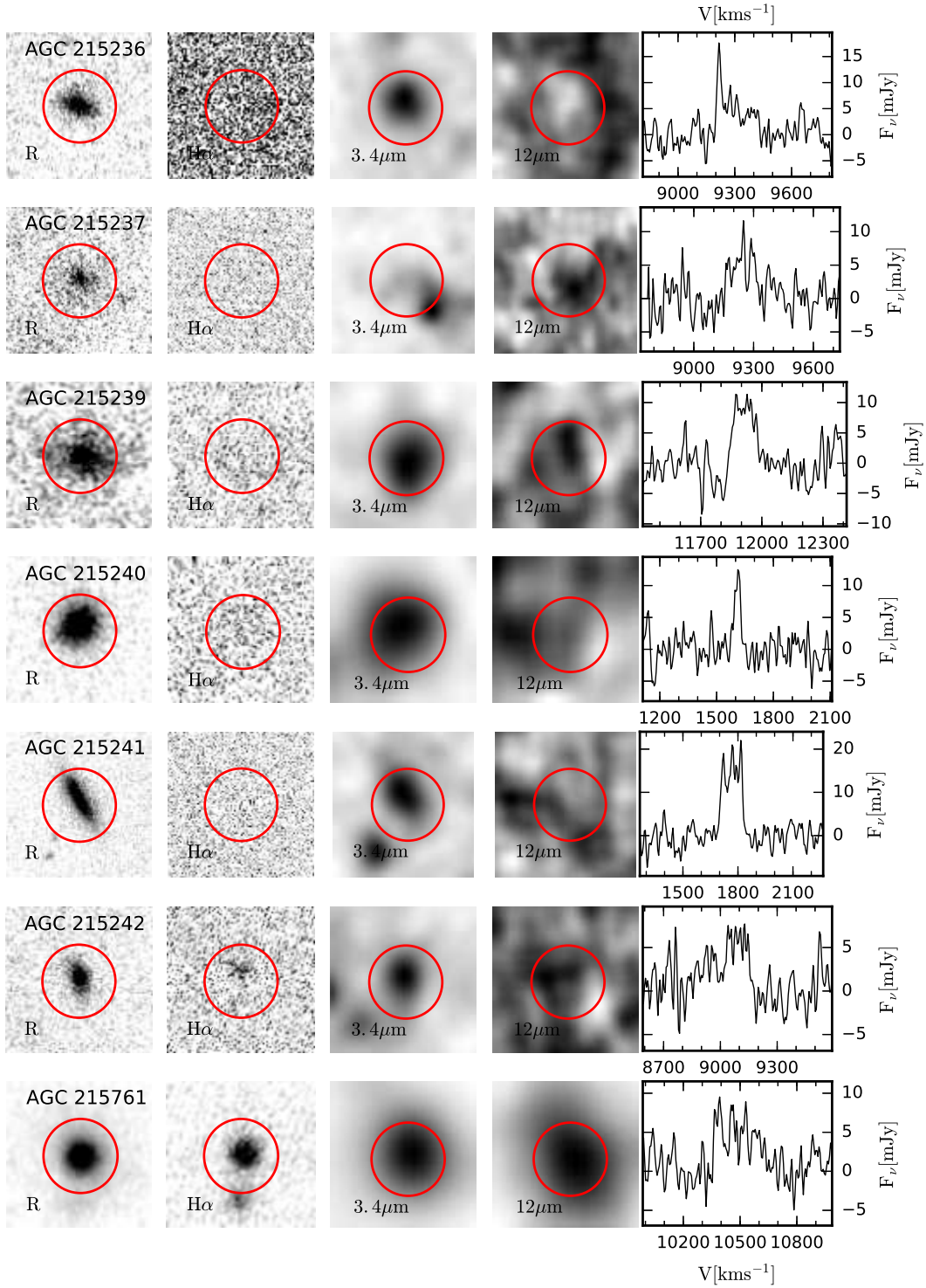


Figure A.1. (Continued)

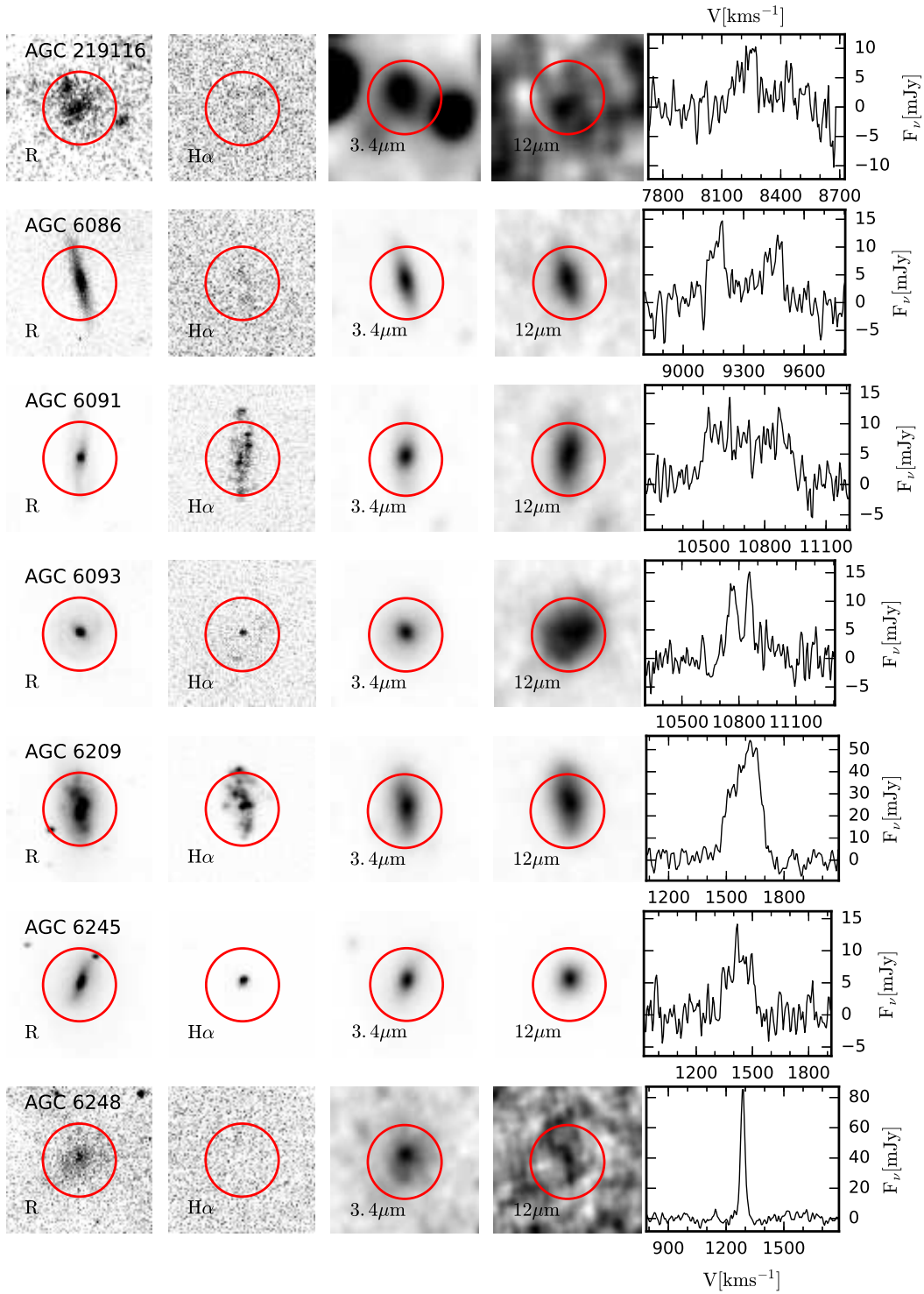


Figure A.1. (Continued)

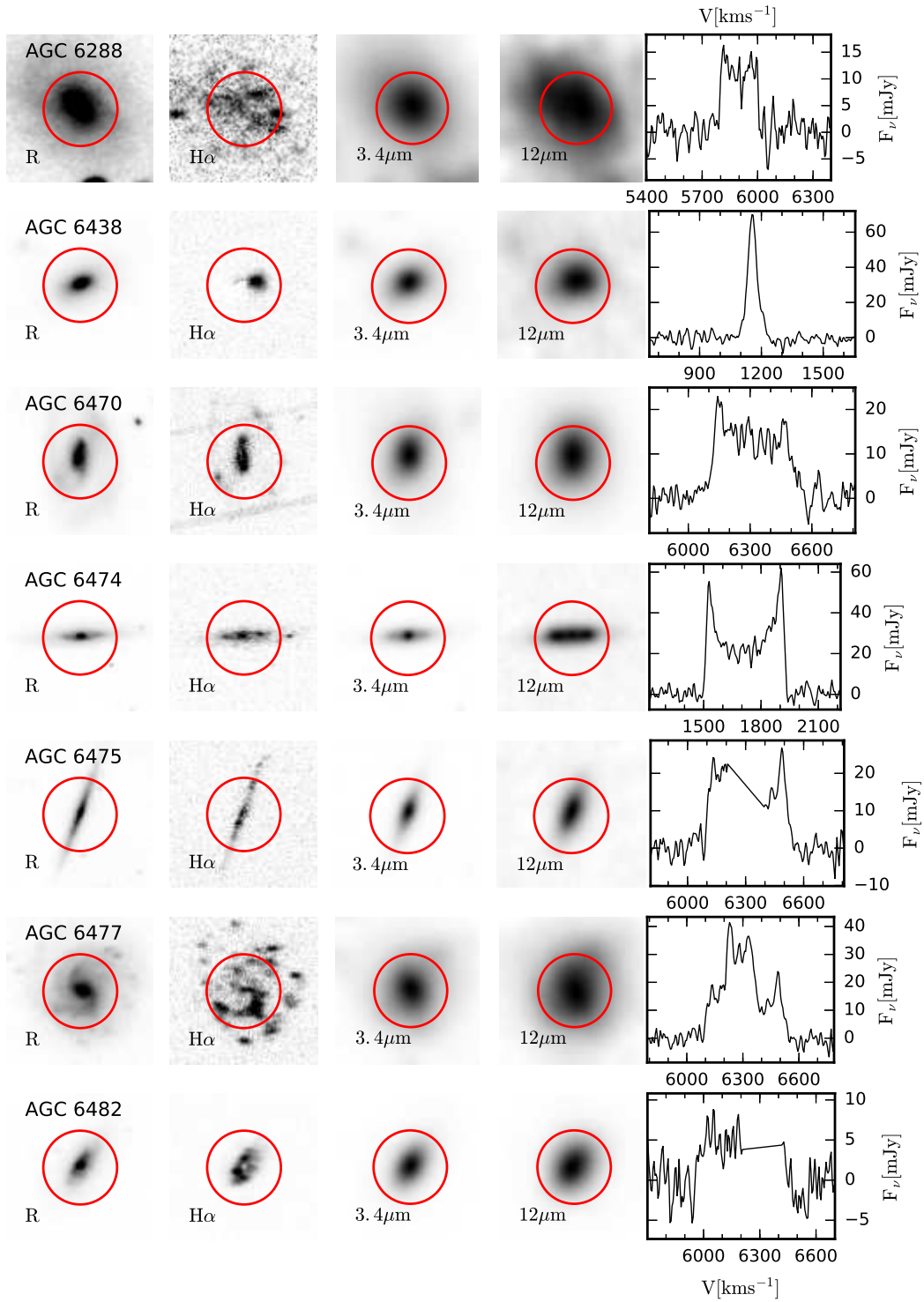


Figure A.1. (Continued)